Supporting Information for "Tidally induced flow variations in Rutford Ice Stream, West Antarctica, inferred from continuous synthetic aperture radar observations"

B. Minchew[1,2], M. Simons[1], B. Riel[1], and P. Milillo[3,4]

Corresponding author: B. M. Minchew, British Antarctic Survey, High Cross, Madingley Road, Cambridge CB3 OET, UK. (bremin15@bas.ac.uk)

[1]Seismological Laboratory, California Institute of Technology, Pasadena, California, USA.

[2]Now at British Antarctic Survey, Cambridge, UK

[3]School of Engineering, University of Basilicata, Potenza, Italy.

[4]Now at Jet Propulsion Laboratory, Division of Geological and Planetary Sciences, California Institute of Technology, Pasadena, California, USA.

Contents of this file

1. Text S1 to S2
2. Tables S1 to S2
3. Figures S1 to S20

Additional Supporting Information (files uploaded separately)

1. Captions for Movies S1 to S2 (movie files are separate, their filenames are given above the respective caption)

Introduction

In the following sections we discuss the method validation and the formal error estimates and other quality metrics for the inferred time-dependent, 3D velocity fields. Section S1 provides greater detail on the synthetic ice stream model and battery of tests conducted using the synthetic ice stream to demonstrate the effectiveness of our proposed method for inferring time-dependent, 3D velocity fields. We include a thorough discussion of sources of error and the optimal family of sinusoidal terms that adequately capture ice flow given our dataset. Section S2 provides formal error estimates and other quality metrics, such as comparisons with existing data and spatial derivatives, corresponding to the results presented in the main text for Rutford Ice Stream (RIS), West Antarctica. Figures are referenced throughout the main text and in Sections S1 and S2. Captions for two movies of the time-dependent, 3D velocity fields are provided first.

Movie 1:

file: rutford_tidal_up_trans.mp4

Vertical motion on Rutford Ice Stream inferred from 9 months of continuous SAR observations collected from CSK. (a) Vertical position of the ice shelf relative to mean elevation (positive values are up). (b) Relative vertical position of the ice shelf along the blue transect in (a). (c) Modeled vertical tidal displacement over the ice shelf using amplitude and phase values given by CATS2008a_opt [*Padman and Fricker*, 2005]. Relative positions of the ice shelf combine inferred amplitude and phase values for the lunar semi-dirunal (M_2) and lunar diurnal (O_1) periods with estimated amplitude and phase values for the solar semi-diurnal (S_2) tidal constituent to give an estimate of the total motion of the ice shelf. Estimates of amplitude and phase values at the S_2 period for any given spatial position are calculated by assuming that the amplitude and phase ratios between the M_2 and S_2 tidal constituents—as given by CATS2008a_opt at a position coincident with a GPS station located on the ice shelf [*Gudmundsson*, 2006]—are spatially constant.

Movie 2:

file: rutford_tidal_hvel_only.mp4

Horizontal ice flow on Rutford Ice Stream inferred from 9 months of continuous SAR observations collected from CSK. (a) Total horizontal flow. Colormap indicates horizontal speed and vectors give flow direction. (b) Horizontal M_{sf} (14.77-day period) flow variability. Colormap indicates the along-flow component (negative values oppose flow) while vectors indicate direction of tidal variability. Contour lines give secular horizontal speed in 20 cm/day increments. (c) Modeled vertical tidal displacement over the ice shelf (same as in Movie 1c).

S1. Tests with synthetic data

To explore the methods developed in the previous section, we generated a synthetic ice stream covering the geographic region of RIS (Fig. 1). The synthetic ice stream is symmetric about the central flowline with half-width w and length L. We compute the velocity profile using an idealized ice stream model [*Raymond*, 1996; *Cuffey and Paterson*, 2010] and place grounded ice in the north and an ice shelf in the south with a smooth transition in vertical tidal influence between grounding and floating ice. The synthetic ice stream can be summarized as:

$$\mathbf{v}_{syn}(x,y,t) = \left[\begin{array}{ccc} v_{syn}^{\hat{e}} & v_{syn}^{\hat{n}} & v_{syn}^{\hat{u}} \end{array}\right]^T \tag{S1a}$$

$$v_{syn}^{\hat{e}}(x,y,t) = 0 \tag{S1b}$$

$$v_{syn}^{\hat{n}}(x,y,t) = s_v \frac{x}{L}\left[-v_{ideal} + P^{\hat{n}}\right] \tag{S1c}$$

$$v_{syn}^{\hat{u}}(x,y,t) = s_v \frac{x-L}{10L} v_{ideal} + P^{\hat{u}} \tag{S1d}$$

$$P^{\hat{\zeta}}(x,y,t) = \sum_{i=1}^{k} \Gamma_i^{\hat{\zeta}}\left[\sin\left(\omega_i t_a + \phi_i^{\hat{\zeta}}\right) - \sin\left(\omega_i t_b + \phi_i^{\hat{\zeta}}\right)\right] \tag{S1e}$$

$$\Gamma_i(x,y) = \frac{v_{ideal}}{v_{ideal}^{center}}\left[\begin{array}{ccc} 0 & \tilde{a}_i^{\hat{n}} & \tilde{a}_i^{\hat{u}}\Upsilon \end{array}\right]^T \tag{S1f}$$

$$\Upsilon(x,y) = \left\{1 + \tanh\left[k_h\left(x - 0.6L\right)\right]\right\}/2 \tag{S1g}$$

$$v_{ideal}(y) = v_{ideal}^{center}\left[1 - \left(1 - \frac{y}{w}\right)^{n+1}\right] \tag{S1h}$$

$$v_{ideal}^{center} = \frac{2Aw}{n+1}\left[\tau_d \frac{w}{h}\left(1 - \frac{\tau_b}{\tau_d}\right)\right]^n \tag{S1i}$$

where Υ defines the ice shelf such that ice in the northern 60% of the ice stream is grounded, $k_h = 10^{-|\log_{10}(L) - 0.8|}$ dictates the sharpness of the grounding zone transition, $\tau_d = \rho g h \alpha$ is the gravitational driving stress and x and y are spatial coordinates defined such that $0 \leq x/L < 1$ and $0 \leq y/w \leq 2$. Parameter definitions and values, given in Table S1, are constant in space and time. Note that the synthetic ice stream is flowing due south and its maximum vertical speed is 10% of the maximum horizontal speed (Figs. S1Sa–Sf and S3Sa–Sf).

Horizontal and vertical components of the simulated ice stream contain 11 tidal constituents. In order to make our synthetic ice stream flow as much like RIS as possible, we assigned the amplitude and phase values using results from more than 2 years of GPS measurements collected on RIS and reported by *Murray et al.* [2007, Table 1]. For convenience, we summarize these values in Table S2. Amplitudes vary over the grounded ice in the same manner as the velocities and are constant over the central ice shelf. Because there is only slight latency in tidal response as a function of distance upstream of the grounding line, we made phase values spatially constant [*Gudmundsson*, 2006].

We observed the synthetic ice stream with the same set of viewing geometries as we use for RIS. We added zero-mean Gaussian white noise with a 2-cm standard deviation, approximately twice the typical noise level in the actual data, to each offset field. Importantly, we do not weight the synthetic data by the additive noise as we do the actual data. This means our synthetic observations have levels of unaccounted noise that are roughly double the formally estimated noise levels in the data. We do this to demonstrate the robustness of our inversion method to observational noise.

S1.1. Results and discussion

Results from multiple synthetic tests provide 3D secular velocity values, a suite of amplitude and phase values corresponding to the user-defined set of sinusoidal functions, and corrections to a synthetic DEM. While formal error estimates are also included, we detail only the components of the noise-sensitivity matrix, $\mathbf{S}$ (Eq. 28), and reserve discussion of $\widetilde{\mathbf{C}}_m$ for the observed data. The components of $\mathbf{S}$ are functions of only the set viewing geometries at a given point and so are identical for both the synthetic and observational data.

We conducted numerous tests using different families of sinusoidal functions, limiting the potential members to only those periods that are short enough to be adequately sampled by our observations and that are not obviously aliased by the near-integer-day repeat time between CSK observations. Data presented here were collected over 9 months, so the first condition eliminates the solar semi-annual, S_{sa}, and annual, S_a, constituents. Times between CSK observations are always within seconds of being integer days, thus aliasing the solar semidiurnal constituent, S_2, and the lunar semidiurnal constituent, K_2, along with the diurnal solar—S_1 and P_1—and lunar, K_1, constituents. Valid members are then the lunar semidiurnal, M_2, and diurnal, O_1, constituents; the lunisolar fortnightly M_f and the lunisolar synodic fortnightly M_{sf} constituents; and the lunar monthly M_m constituent.

We inferred 4D velocity fields for every combination of valid tidal constituents, including the DEM correction term in each, using the synthetic ice stream described in Eqs. S1a–S1i and Table S2, with $\kappa_p = 10$ m^{-2} (Eq. 18 in the main text), a value derived through trial and error. Here, we present a representative set of 5 tests. Results from each test occupy unique rows in Figs. S1–S8 with the tidal constituents used in the inversion labeled on the left side. Left columns in Figs. S1–S3 contain the secular velocities along the respective spatial dimension and other column positions correspond to the tidal constituent designated in the top rows. Results from the 4D inversion tests are given as differences between the inferred and true values.

S1.1.1. Secular velocity fields

Our synthetic ice stream flows due south with maximum southerly speeds of approximately 1 m/day (Fig. S1), and zero easterly speeds (Fig. S2). Southerly flow is captured within 2% of the synthetic ice stream flow speed and easterly velocities are near zero in all well-observed areas in all 4D inversion tests. When M_2 tides are included in the inverse model, estimated north velocities are well within 1% of the actual velocity, and easterly velocities remain near zero. These results suggest that the horizontal velocity fields in the observational data will have true errors that are within 5% of the expected values.

In practice, the up component of the velocity field can be difficult to obtain for a variety of reasons related to limited data, minimal viewing geometry diversity, and varying environmental conditions [e.g. *Joughin*, 2002; *Rignot et al.*, 2011; *Minchew et al.*, 2015]. Owing to the quantity of data and diversity in viewing geometries afforded by the CSK observations, we are able to fit the vertical velocity component to within 2% over grounded ice and within 5% or 20% over the ice shelf, depending on which tidal constituents are included in the inverse model (Fig. S3). The largest absolute errors in vertical speed occur over the ice shelf when M_2 is not included in the inverse model (Figs. S3T2a and S3T1a) because M_2 is the largest contributor to vertical motion by at least a factor of 3. Given the sampling frequency and repeat time between CSK observations, not including M_2 in the inverse model causes some of the high-frequency vertical motion to bleed into the secular velocity term.

S1.1.2. Sinusoidal amplitudes

The horizontal tidal displacements give generally better results over grounded ice relative to floating ice (Figs. S1 and S2). As with the secular velocity results, we see a marked improvement in the inferred horizontal periodic amplitudes when M_2 is included in the inverse model. We attribute this improvement in overall accuracy to the fact that SAR provides measurements along either the oblique radar LOS or along the purely horizontal azimuth direction. Due to the satellite headings, north velocity components are constrained primarily by LOS observations, which contain both horizontal and vertical components. Excluding M_2, the largest vertical tidal constituent, causes some of the unaccounted vertical motion to manifest in the horizontal fields. When M_2 is included, errors in M_{sf}, the period with the largest influence in horizontal ice flow, are typically less than 5%. O_1, and to a lesser degree M_2, horizontal components have large errors relative to their true amplitudes, but small absolute errors. Errors in O_1 diminish as long-period constituents, M_f and M_m, are added to the inverse model while misfits in M_2 and M_{sf} are largely unaffected by the presence of M_f and M_m. Given the sizable misfits in M_f and M_m, it is likely that improvements in O_1 occur because misfits are shifted to the longer period components as a consequence of including $\mathbf{C}_m$. In terms of fitting time-varying horizontal velocity, these results suggest that the optimal family of periodic functions is M_2, O_1, and M_{sf}. Accounting for all misfits with this family of periodic functions, we should conservatively expect to observe the horizontal ice flow variability on RIS to within 10% of the true signal.

Vertical tidal displacements have the largest amplitudes, by more than an order of magnitude compared with the largest horizontal amplitudes, and the inferred sinusoidal amplitudes are correspondingly well fit when M_2 is included in the inverse model (Fig. S3). When M_2 is excluded from the inversion, misfits in the vertical components are an order of magnitude or more larger than the true value because the inversion is compensating for much of the high-frequency vertical motion using the available low-frequency functions and the secular vertical velocity. When M_2 and O_1 occupy the inverse model, errors in the respective inferred amplitudes rarely exceed 2% in M_2 and 3% in O_1 within well observed areas. Errors at fortnightly and monthly periods approach 50% in some areas over the ice shelf, but because the amplitudes of the true low-frequency signals are small, the absolute values of these errors are negligible relative to the amplitude of the M_2 displacement. Over grounded ice, where vertical amplitudes at all tidal periods are zero, there are virtually no erroneous inferred values except on the edges of the observational domain where we have limited viewing geometry diversity. Based solely on misfits in vertical displacement, we contend that the M_2, O_1, and M_{sf} family of tidal frequencies affords the best solution for the given observational dataset.

S1.1.3. Sinusoidal phase values

Inferred phase values for the periodic functions match the respective synthetic components to well within 10° in all velocity components in regions where the amplitude is large and the amplitude misfit is small (Figs. S4–S5). Here we exclude phase values for the east component because true and inferred amplitudes are near zero. We retain the complete observational domain in both the north an up components to illustrate the pseudo-random behavior of inferred phase in areas with small or zero amplitude. The phase results in areas with sufficiently large amplitudes are consistent with the secular velocity and periodic amplitudes in that the smallest misfits in all nonzero-amplitude components are achievable only when M_2 is included in the inversion. Of particular note is that large and spatially random errors occur in the inferred north component of M_{sf} when M_2 is not included in the inversion, a finding that has consequences for future mission planning with satellite platforms that offer less frequent data acquisitions than CSK. It is unclear as to why M_f phase values are consistently shifted by approximately $-90°$ and M_m phase by approximately 180° in both the north and up components. The most likely explanation involves a combination of having complementary periods to the period with the strongest horizontal signal (M_{sf}), relatively little sampling given the $\lesssim$ 9-month duration of the CSK acquisitions, and viewing-geometry-induced covariance between the north and up components, which is discussed in the next paragraph and would account for the two periods having similar errors in both spatial dimensions. Given the large misfits in M_f and M_m phases, we conclude that the phase misfits support our previous assertions that the overall best results are attainable using the M_2, O_1, and M_{sf} family of tidal frequencies, though it is instructive to consider how the noise sensitivity changes as a function of which tidal periods are included in the inverse model.

S1.1.3. Noise-sensitivity matrix elements

Noise-sensitivity matrix, **S**, elements provide information about the conditioning of the design matrix, which is directly related to how well the observations constrain ice motion (Figs. S6–S8). Higher values in the **S** elements indicate poorer constraints on motion. In our observations, all three secular velocity components are tightly constrained with values $\sim 10^{-3}$. The poorest constraints on secular velocity are in the north component because the satellite headings in all 32 flight tracks are within 45° of west and are rarely less than 20° from west, meaning that the majority of LOS displacement measurements, which are sensitive to vertical and horizontal motion, are primarily oriented north while all measurements of displacement in the purely horizontal azimuth direction are primarily oriented east. A notable consequence of this viewing geometry is that there is strong positive (> 0.5) correlation between errors in the north and up components everywhere in the observational domain while errors in the east component, which are constrained primarily by purely horizontal displacement fields, are uncorrelated with the north and up components (not shown).

Tidal components are not as well constrained as the secular velocity components, but still have relatively low sensitivity to measurement noise (Figs. S6–S10). This low noise sensitivity is indicated by the fact that all tidal component amplitudes have corresponding **S** elements that are less than unity. The highest sensitivities in the tidal amplitudes occur in the M_2 and M_{sf} components, with the addition of M_2 imbuing M_{sf} with greater noise sensitivity in all components. This causal relationship arises from the complementary periods for M_2 and M_{sf} tides and manifests in the noise sensitivity of inferred phase values.

Inferred sinusoidal amplitude is the most important determinant of the sensitivity of the respective inferred phase values to measurement noise because sensitivities in phase are inversely proportional to amplitude squared (Eq. 29 and Figs. S9–S10). This proportionality is most important in this case for inferred horizontal M_{sf} phase values, which are ~ 100 over the ice stream when M_2 is included (Fig. S9), despite having accurate inferred values (Fig. S4). Phase values for the vertical M_2 and O_1 over the ice shelf have low noise sensitivity owing to large inferred amplitudes. This amplitude dependence in the sensitivity of phase values to instrument noise mean that areas with small expected amplitudes need to have a large number of observations and good azimuthal coverage in viewing geometries to yield reliable inferred phase values.

S1.1.3. DEM corrections

We inferred DEM corrections for all tested combinations of tidal constituents, but present results for only the M_2, O_1, and M_{sf} family (Fig. S11). Though we only give results for synthetic δz_d amplitude of 100 m (Fig. S11a), we tested numerous amplitudes and note that the misfit of inferred δz_d (Fig. S11b) is independent of the true δz_d amplitude. Over most of the grounded stagnant ice, where the synthetic signal is due only to residual topography, δz_d, inferred DEM corrections are virtually identical to the true value where noise. Where ice is flowing, misfits between true and inferred δz_d are larger, though still relatively small over the grounded ice. Over the ice shelf, where there is far more vertical motion than over grounded ice, inferred corrections to the DEM feature large, spatially patchy misfits. These large misfits arise from misfits in vertical and horizontal motion and are sensitive to non-ideal viewing geometries and measurement noise.

S1.1.4. Fidelity of inferred velocity fields

The tidal constituent with the greatest impact on the accuracy of the inferred 4D velocity fields is M_2. M_2 tides have the largest amplitudes and are not aliased by the satellite observational frequency, which means M_2 contributes significantly to the observed temporal variations in ice flow. The importance of M_2 is exacerbated by the satellite viewing geometries. Half of our observations are along the westerly azimuth vectors that have no sensitivity to vertical motion. The other half of our observations are collected along the radar LOS and are sensitive to horizontal (primarily northerly in this case) and vertical motion. None of our observations are purely vertical, which means that the strong vertical motions caused by M_2 manifest in both vertical and horizontal velocity components unless they are properly captured by the inverse model. Synthetic results described here for all inferred values show that it is essential to include M_2 in the inverse model in order to properly constrain both vertical and horizontal motion over the ice shelf an in the vicinity of the grounding line. Because we based the synthetic ice stream on GPS observations collected on RIS, we expect the results from the synthetic data to inform our observational results.

S1.2. Conclusions from synthetic tests

The synthetic tests presented here show that our method can infer temporal ice flow variability to within 10% of the true values in vertical and horizontal dimensions. These tests were carried out using a synthetic ice stream whose prescribed temporal ice flow variability matches previously published GPS observations collected on RIS Ice Stream, West Antarctica [*Murray et al.*, 2007]. Synthetic results showed that the posterior model that yields the overall most accurate results contains the 3D secular velocity and 3D sinusoidal function corresponding to the M_2, O_1, and M_{sf} family of tidal constituents. We find that including the M_2 period is essential for accurate estimates of ice flow over the shelf, but note that this finding is unique to the Filchner-Ronne region because of the anomalously strong semi-diurnal tides in this area. We postulate that accurately inferring vertical motion at the primary observable tidal frequencies is necessary wherever accurate time-dependent 3D velocity fields are desired over an ice shelf.

S2 Additional RIS results and formal error estimates

We use all available SAR acquisitions collected by CSK from August 2013–April 2014. During processing, we discovered that scene pairs with long interim times rarely produced coherent displacement fields, so we only applied offset-tracking to scene pairs with interim times < 10 days. This processing scheme yielded 4448 displacement fields, of which 1644 are coherent enough over RIS to be useful for this analysis (Fig. S15). The prime reasons for the low success rate are the low SNR of the amplitude images caused by low radar backscatter in dry snow combined with the ephemeral nature of the mostly flat snow surface in regions that have experienced little strain. Where cumulative strain is high, such as in the margins, or surface slopes are steep, displacement fields are more likely to be coherent (Fig. S15).

S2.1 Secular horizontal velocity and strain rate fields

S2.1.1 Comparing secular horizontal velocity with previous results

Comparison of our inferred horizontal velocity fields with results from *Rignot et al.* [2011] shows consistency over the extent of the CSK observational domain (Fig. S16). Positive values indicate slower speeds in our estimates and occur predominately along the eastern ice stream margin both inland and seaward of the grounding line. Ice within the central trunk of RIS and within the central bend of the grounding line is moving approximately 10–15% faster in our data relative to *Rignot et al.* [2011]. But the most significant differences in terms of amplitude and width in the transverse-flow direction occur along the two ice stream margins and particularly the inboard (northeast) curve on the ice shelf. Large differences are also present in the eastern margin for approximately 75 km upstream of the grounding zone. Differences in horizontal speed taper off beyond 100 km inland of the grounding zone in the eastern margin, becoming slightly more pronounced in the northern extent of our observational domain. Differences in horizontal speed are less pronounced in the western margin and have the opposite sign as the relative speeds in the eastern margin. There is notably faster ice flow in our data, approximately 25 cm/day faster, within 30 km upstream of the grounding zone and markedly faster ice in our data along the western margin for approximately 50 km immediately downstream of the grounding zone. The most likely explanation for the disparity in shear margin speeds between the two datasets is the significant difference in spatial resolution. The CSK-derived velocity fields have an order of magnitude (≈ 45 m) finer resolution than the *Rignot et al.* [2011] data (450-m grid spacing). Finer spatial resolution combined with the relatively high SNR ratio in the CSK data compared with the older satellite data used by *Rignot et al.* [2011] allows sharper definition of the shear margins.

S2.1.2 Velocity field formal errors

Formal errors in the secular velocity fields are typically less than 5% of the flow speed (Fig. S17a–c). Owing to the CSK viewing geometries, the north component generally has the highest absolute errors while the up component has the highest errors relative to its speed. The east component has the lowest errors because displacement fields that constrain the east component are azimuth offsets, which lie entirely in the horizontal plane, and are oriented within 45° of west. In other words, the east component is largely independent from the other two components and essentially has its own set of displacement fields to constrain the east motion. The north and up components, on the other hand, share the LOS displacement fields, resulting in strongly correlated errors (Fig. S17e–f). In general, formal errors are minimized at mid-latitudes within the observational domain because those areas have the highest number of scenes available for the inversion. As with any data stacking method, the uncertainly in inferred velocity fields decreases approximately as the square root of the number of scenes [*Minchew et al.*, 2015; *Simons and Rosen*, 2015].

S2.1.3 Secular strain rate fields

Surface velocity fields provide direct estimates of areal strain rates, which can be related to stress through a constitutive relation. Furthermore, strain rate fields are the spatial derivatives of velocity fields and therefore provide a measure of random spatial noise in the velocity fields.

Inferred velocity fields include secular and sinusoidal components of displacement, so we define the total velocity at a given position and time as:

$$\mathbf{v}\left(x, y, t\right) = \mathbf{v}'(x, y) + \sum_{i=1}^{k} \mathbf{v}_i''(x, y, t) \tag{S2}$$

where:

$$\mathbf{v}_i'' = \omega_i \begin{bmatrix} \cos\left(\omega_i t + \phi_i^{\hat{e}}\right) \\ \cos\left(\omega_i t + \phi_i^{\hat{n}}\right) \\ \cos\left(\omega_i t + \phi_i^{\hat{u}}\right) \end{bmatrix} \tag{S3}$$

The Jacobian of the velocity field can be decomposed in to a symmetric strain-rate tensor and an antisymmetric rotation rate tensor whose components are defined respectively as:

$$\dot{\varepsilon}_{\hat{x}\hat{y}} = \frac{1}{2}\left(\frac{\partial v_{\hat{x}}}{\partial \hat{y}} + \frac{\partial v_{\hat{y}}}{\partial \hat{x}}\right) \tag{S4}$$

$$\dot{\mathrm{w}}_{\hat{x}\hat{y}} = \frac{1}{2}\left(\frac{\partial v_{\hat{x}}}{\partial \hat{y}} - \frac{\partial v_{\hat{y}}}{\partial \hat{x}}\right) \tag{S5}$$

where $\hat{x}$ and $\hat{y}$ are orthogonal coordinate dimensions. From Eqs. S2–S4 we can derive the total time-dependent strain-rate tensor components as:

$$\dot{\varepsilon}_{\hat{x}\hat{y}} = \dot{\varepsilon}'_{\hat{x}\hat{y}} + \dot{\varepsilon}''_{\hat{x}\hat{y}} \tag{S6a}$$

$$\dot{\varepsilon}'_{\hat{x}\hat{y}} = \frac{1}{2}\left(\frac{\partial \mathrm{v}'_{\hat{x}}}{\partial \hat{y}} + \frac{\partial \mathrm{v}'_{\hat{y}}}{\partial \hat{x}}\right) \tag{S6b}$$

$$\dot{\varepsilon}''_{\hat{x}\hat{y}} = \frac{1}{2}\sum_{i=1}^{k}\omega_i\Bigg[\cos\left(\omega_i t + \phi_i^{\hat{x}}\right)\frac{\partial a_i^{\hat{x}}}{\partial \hat{y}} + \cos\left(\omega_i t + \phi_i^{\hat{y}}\right)\frac{\partial a_i^{\hat{y}}}{\partial \hat{x}} - a_i^{\hat{x}}\sin\left(\omega_i t + \phi_i^{\hat{x}}\right)\frac{\partial \phi_i^{\hat{x}}}{\partial \hat{y}} - a_i^{\hat{y}}\sin\left(\omega_i t + \phi_i^{\hat{y}}\right)\frac{\partial \phi_i^{\hat{y}}}{\partial \hat{x}}\Bigg] \tag{S6c}$$

where $\dot{\varepsilon}'_{\hat{x}\hat{y}}$ and $\dot{\varepsilon}''_{\hat{x}\hat{y}}$ are the secular and periodic strain rates, respectively. Similarly, we can decompose the rotation rate tensor into secular and periodic tensors: $\dot{\mathrm{w}}_{\hat{x}\hat{y}} = \dot{\mathrm{w}}'_{\hat{x}\hat{y}} + \dot{\mathrm{w}}''_{\hat{x}\hat{y}}$. The areal divergence of velocity is equal to the trace, or first tensor invariant, of the strain rate tensor, which is nonzero in areas where the apparent volume of ice is changing, due to damage, or in areas which vertical motion, which may be balanced by mass accumulation or ablation. Effective strain rate, $\dot{\varepsilon}_e$, is calculated from the second invariant of the strain rate tensor, $\dot{\boldsymbol{\varepsilon}}$, and is defined as:

$$\dot{\varepsilon}_e = \sqrt{\left[\mathrm{tr}\left(\dot{\boldsymbol{\varepsilon}}\dot{\boldsymbol{\varepsilon}}\right) - \mathrm{tr}\left(\dot{\boldsymbol{\varepsilon}}\right)^2\right]/2} \tag{S7}$$

Assuming $\dot{\varepsilon}'_{\hat{x}\hat{y}}$ and $\dot{\varepsilon}''_{\hat{x}\hat{y}}$ are uncorrelated, we can decompose effective strain rate into secular and period terms as:

$$\dot{\varepsilon}_e = \dot{\varepsilon}'_e\sqrt{1 + \left(\dot{\varepsilon}''_e/\dot{\varepsilon}'_e\right)^2} \tag{S8}$$

Ice flow over the grounded ice in our observational domain is primarily due to slip at the ice-bed. Velocity is constant with depth when ice is afloat. Consequently, $\dot{\varepsilon}_{\hat{z}\hat{z}} = 0$ at the surface—which is the commonly applied stress boundary condition at the free surface in numerical models. Furthermore, $2\dot{\varepsilon}_{\hat{x}\hat{z}} \approx 2\dot{\varepsilon}_{\hat{z}\hat{x}} \approx \partial u_{\hat{z}}/\partial \hat{x}$, where $\hat{x}$ is a horizontal dimension and $\hat{z}$ is vertical [e.g. *Morlighem et al.*, 2013]. The vertical rotational tensor components are proportional to the respective vertical strain rate components such that $\dot{w}_{\hat{x}\hat{z}} = -\dot{w}_{\hat{z}\hat{x}} = -\dot{\varepsilon}_{\hat{x}\hat{z}}$. These relationships and the assumption of a stress-free ice surface result in six unique, nonzero strain and rotation rate tensor components, plus the two strain rate tensor invariants (Fig. S18). We filtered each of these eight strain fields using a Gaussian filter with a 6-standard-deviation width of 4 km, or approximately 2 ice thicknesses.

S2.1.3.1 Effective strain rate

RIS's lateral margins are delineated by high effective and shear strain rates. These strain rates are well resolved everywhere in the observational domain (Fig. S18). Secular effective strain rates are highest in the margins of the ice stream in most of the observational domain. The highest effective strain rates generally occur in areas overlying steep bathymetry, where the ice stream narrows, and where there are no incoming tributary glaciers. Effective strain rates are low in the margin within an approximately 60-km long region in the western margin of the ice shelf that aligns with MG, which is flowing from the southwest (Fig. S18a). In this area, ice from MG merges with the main ice stream flow, reducing effective strain rates.

S2.1.3.2 Horizontal velocity field divergence

Divergence in the secular velocity field is small within most of the ice stream (Fig. S18b), consistent with the commonly applied assumption that ice is incompressible, and high in some localized areas and within portions of the shear margin. Where divergence is high and spatially localized, we expect the ice to be damaged due to local changes in ice volume (positive values denote extension and negative values indicate compression) or to have relatively steep ice surface gradients resulting from localized uplift or downwelling caused by nonzero spatial gradients in basal shear traction or topography. Damage often appears as bright areas in radar amplitude images, because damaged areas tend to scatter more energy back to the radar than non-damaged areas, while steep surface slopes will appear in optical imagery but may be less apparent in radar images because radar penetrates to a wavelength-dependent depth of order meters below the ice surface [*Ulaby et al.*, 1986; *Rignot et al.*, 2001]. We observe coincident areas of high divergence in the inferred velocity fields and high radar backscatter amplitude in CSK amplitude images (not shown) and the RADARSAT-1 AMM-1 mosaic [*Jezek et al.*, 2013]. Areas of modest, but non-zero, divergence spread over several ice thicknesses are present in the upstream extent of the observational domain and are coincident with hummocky features in the MODIS mosaic of Antarctica 2009 (MOA) [*Haran et al.*, 2005; *Scambos et al.*, 2007; *Haran et al.*, 2014]. Strong localized divergence is manifest near the eastern shear margin in the upstream extent of the observational domain where flowing ice first encounters the Filchner Promontory, the elongated high in basal topography that forms most of RIS's eastern boundary. Approximately 40 km upstream of the grounding zone and near the center of the ice stream trunk we observe high velocity divergence localized in an area not more than a few km across. This feature is present as an isolated region of downwelling in the vertical velocity field and is coincident with localized stiff basal sediments and a prominent bathymetric ridge [*King et al.*, 2009; *Smith and Murray*, 2009; *Smith et al.*, 2015]. Within the grounding zone, we observe localized high velocity divergence within the u-shaped bend, approximately 3 km southwest of the downstream extent of the grounding zone bend, and in the western ice stream margin directly across flow from the grounding zone bend where the bathymetric channel protrudes slightly into the the path of the ice flow. Along the eastern margin on the ice shelf, we see extensional strain inboard and compressional strain outboard of the curve. Divergence in this part of the shelf is beaded, a pattern that is reflected in the morphology shown in the underlying MOA imagery. This section of high divergence is located directly across flow from MG where the bathymetry is relatively flat, the shear margin is poorly defined, and, as we later show, the width of the ice stream changes at fortnightly periods more dramatically than anywhere else in the observational domain.

S2.1.3.3 Normal strain rates

Along- and transverse-flow deviatoric strain rate components have some of the highest values in the shear margins where bathymetry is steep and where tributary glacier meet the main ice stream. But the highest deviatoric normal strain rates are located in the eastern shelf margin where strong divergence is observed. Along flow normal strain rates are oriented against the flow in this part of the shear margin while transverse flow normal stresses act outward. In both normal strain components, we note a rapid sign change in the eastern shear margin immediately downstream of MG where the bathymetry begins to shallow to a nunatak just beyond the observational domain (approximately 79.3 °S, 81.5 °W).

S2.1.3.4 Lateral shear strain and rotation rates

Lateral shearing is strong in the ice stream margins and diminishes to near zero within the main trunk of the ice stream because of the nonlinear rheology of ice and shear heating, damage, and ice fabric reorientation in the margins (Fig. S18e) [e.g., *Echelmeyer et al.*, 1994; *Hudleston*, 2015]. Lateral shear rates are high where the ice stream is bounded by steep bathymetry, with maximum values located in areas where bathymetry is steepest along both the east and west margins. Shearing is relatively low in the upstream eastern margin, where bathymetric slopes are shallow, and in the ice shelf margins. The lowest shear rates within the margins are coincident with the suture zone where MG intersects the main flow from RIS. Shearing increases, relative to its upstream value, as ice approaches the nunatak at 79.3 °S, 81.5 °W. The first-order thickness of the shear margins everywhere in the ice stream varies as the inverse of the shear strain rate and the thinnest shear margins are co-located with the highest secular horizontal speeds. Lateral rigid body rotation rates are highest in the shear margins and behave much like lateral shear strain (Fig. S18f). Due to the relatively small normal strain rates, lateral solid body rotation rates are approximately half the coincident lateral shear strain rates.

S2.1.3.5 Vertical strain rates

Along- and transverse-flow vertical shear strain rates have lower values in general than all other strain and rotation rate components (Fig. S18g–h). Like lateral shear strain rates, both vertical shear strain rate components are typically near zero along the central trunk. Unlike lateral shear strain rates, the vertical shear components have high frequency features of interest. In the upstream region, along-flow vertical shearing indicates hummocky patterns similar in character to those observed in MOA. Given the broad spatial scales of velocity divergence values in this area, it is likely that they these surface features are due to roughness along the bed. Approximately 40 km upstream of the grounding zone, in the area of downwelling and strong divergence, we observe a strain doublet, which indicates compression on the upstream side of the area of rigid sediment. A complementary doublet that is rotated approximately 90° and has less than a quarter the magnitude, occurs in transverse vertical shear at the same location. In the central bend of the grounding zone, we observe a similar strain doublet. This doublet extends westward from the central grounding zone by approximately 3–5 km into the flow path of ice traversing the grounding zone through the western horn. Along the western margin immediately upstream of the grounding zone, we observe a 10-km-long stretch of strong vertical shearing whose downstream end features a multi-km-scale section of compressive along-flow vertical strain. This same area indicates high transverse vertical strain, owing to the fact that vertical velocity is concentrated in the ice stream margin in this area. High extensive-inboard, compressive-outboard transverse vertical strains are present though half of the observed western ice stream margin and are complemented by slightly higher transverse vertical strain rates in the eastern margin. A broad stretch of moderate transverse vertical strain rates is evident approximately 3 km inboard of the eastern shear margin near the downstream extent of the observational domain.

S2.2 Formal errors in periodic deformation fields

Formal error estimates for amplitude and phase values for all of the vertical and horizontal periodic deformation fields presented in the main text are given in Figs. S19 and S20, respectively. Consistent with the synthetic tests presented in §S1, the formal error estimate is general less than 5%, and rarely exceed 10%, of the inferred value for both M_2 and O_1 period vertical positions (Fig. S19). Formal errors in horizontal amplitude and phase values for the M_{sf} period are generally spatially constant (where inferred amplitude values are larger than approximately 5 cm) and are typically within 10% of the respective inferred phase value or within 0.5 days of the respective inferred phase value.

S2.3 Summary of additional RIS results

Secular and periodic fields described here provide fine spatial resolution ($\sim$100 m) estimates suitable to reconstructing the velocity field of RIS at any time. Our data are in good agreement with previously published velocity fields from *Rignot et al.* [2011], especially when disparities in spatial resolution between the two datasets are taken into account. In addition to providing insight into the spatial distribution of stress, the secular strain rate fields elucidate the low spatial variability in our data. Included with the data, and outlined here, are the components of the model covariance matrix, which show that formal errors are generally small (typically $< 5\%$ and rarely $> 10\%$) relative to the respective inferred field.

References

Cuffey, K. M., and W. S. B. Paterson (2010), *The Physics of Glaciers*, 4th ed., Elsevier.

Echelmeyer, K. A., W. D. Harrison, C. Larsen, and J. E. Mitchell (1994), The role of the margins in the dynamics of an active ice stream, *Journal of Glaciology*, *40*(136), 527–538.

Gudmundsson, G. H. (2006), Fortnightly variations in the flow velocity of Rutford Ice Stream, West Antarctica, *Nature*, *444*(7122), 1063–1064, doi:10.1038/nature05430.

Haran, T., J. Bohlander, T. Scambos, T. Painter, and M. Fahnestock (2005), MODIS Mosaic of Antarctica 2003-2004 (MOA2004) Image Map, *Tech. rep.*, National Snow and Ice Data Center, Boulder, Colorado USA, doi:10.7265/N5ZK5DM5.

Haran, T., J. Bohlander, T. Scambos, T. Painter, and M. Fahnestock (2014), MODIS Mosaic of Antarctica 2008-2009 (MOA2009) Image Map, *Tech. rep.*, National Snow and Ice Data Center, Boulder, Colorado USA, doi:10.7265/N5KP8037.

Hudleston, P. J. (2015), Structures and fabric in glacial ice: A review, *Journal of Structural Geology*, doi:10.1016/j.jsg.2015.09.003.

Jezek, K. C., J. C. Curlander, F. Carsey, C. Wales, and R. G. Barry (2013), RAMP AMM-1 SAR Image Mosaic of Antarctica. Version 2, *Tech. rep.*, National Snow and Ice Data Center, Boulder, Colorado USA, doi:10.5067/8AF4ZRPULS4H.

Joughin, I. (2002), Ice-sheet velocity mapping: a combined interferometric and speckle-tracking approach, *Annals of Glaciology*, *34*(1), 195–201, doi: doi:10.3189/172756402781817978.

King, E. C., R. C. A. Hindmarsh, and C. R. Stokes (2009), Formation of mega-scale glacial lineations observed beneath a West Antarctic ice stream, *Nature Geoscience*, *2*, 585–588, doi:10.1038/ngeo581.

Minchew, B. M., M. Simons, S. Hensley, H. Björnsson, and F. Pálsson (2015), Early melt-season velocity fields of Langjökull and Hofsjökull ice caps, central Iceland, *Journal of Glaciology*, *61*(226), 253–266, doi:10.3189/2015JoG14J023.

Morlighem, M., H. Seroussi, E. Larour, and E. Rignot (2013), Inversion of basal friction in Antarctica using exact and incomplete adjoints of a higher-order model, *Journal of Geophysical Research: Earth Surface*, *118*(3), 1746–1753, doi:10.1002/jgrf.20125.

Murray, T., A. M. Smith, M. A. King, and G. P. Weedon (2007), Ice flow modulated by tides at up to annual periods at Rutford Ice Stream, West Antarctica, *Geophysical Research Letters*, *34*(18), n/a–n/a, doi:10.1029/2007GL031207, l18503.

Padman, L., and H. A. Fricker (2005), Tides on the Ross Ice Shelf observed with ICESat, *Geophysical Research Letters*, *32*(L14503), n/a–n/a, doi:10.1029/2005GL023214.

Raymond, C. (1996), Shear margins in glaciers and ice sheets, *Journal of Glaciology*, *42*(140), 90–102.

Rignot, E., K. Echelmeyer, and W. Krabill (2001), Penetration depth of interferometric synthetic-aperture radar signals in snow and ice, *Geophysical Research Letters*, *28*(18), 3501–3504, doi:10.1029/2000GL012484.

Rignot, E., J. Mouginot, and B. Scheuchl (2011), Ice Flow of the Antarctic Ice Sheet, *Science*, *333*(6048), 1427–1430, doi:10.1126/science.1208336.

Scambos, T. A., T. M. Haran, M. A. Fahnestock, T. H. Painter, and J. Bohlander (2007), MODIS-based Mosaic of Antarctica (MOA) data sets: Continent-wide surface morphology and snow grain size, *Remote Sensing of Environment*, *111*(2–3), 242–257, doi:10.1016/j.rse.2006.12.020.

Simons, M., and P. Rosen (2015), Interferometric synthetic aperture radar geodesy, in *Treatise on Geophysics*, edited by G. Schubert, 2nd ed., pp. 339–385, Elsvier, Amsterdam, doi:10.1016/B978-0-444-53802-4.00061-0.

Smith, A. M., and T. Murray (2009), Bedform topography and basal conditions beneath a fast-flowing west antarctic ice stream, *Quaternary Science Reviews*, *28*(7–8), 584–596, doi:10.1016/j.quascirev.2008.05.010.

Smith, E. C., A. M. Smith, R. S. White, A. M. Brisbourne, and H. D. Pritchard (2015), Mapping the ice-bed interface characteristics of rutford ice stream, west antarctica, using microseismicity, *Journal of Geophysical Research: Earth Surface*, *120*, 1–14, doi:10.1002/2015JF003587.

Ulaby, F. T., R. K. Moore, and A. K. Fung (1986), *Microwave Remote Sensing: Active and Passive*, Artech House, Dedham, Massachusetts.

Table S1. Synthetic ice stream parameters

Parameter	Definition	Value	Unit
A	rate factor in ice flow law[a]	2.4×10^{-24}	Pa^{-3} s^{-1}
α	ice surface slope	0.04	rad.
g	gravitational acceleration	9.81	m s^{-2}
h	ice thickness	1000	m
n	exponent in ice flow law[a]	3	-
ρ	ice density	900	kg m^{-3}
s_v	constant	0.6	-
τ_b	basal shear traction	$0.8\tau_d$	Pa

[a] $\dot{\varepsilon}_e = A\tau_e^n$ where $\dot{\varepsilon}_e$ and τ_e are effective strain rate and stress in the ice, respectively

Table S2. Tidally induced velocity variations included in simulated ice stream flow. Amplitude and phase values are reproduced from *Murray et al.* [2007, Table 1] and inferred from data collected near the R+40 GPS site shown in Fig. 2 of the main text.

Tide	Period (days)	Horizontal amplitude (cm)	Horizontal phase (deg)	Vertical amplitude (cm)	Vertical phase (deg)
K_2	0.498	0.31	163.0	29.1	99
S_2	0.5	0.363	184.0	101.6	115
M_2	0.52	0.259	177.0	156.3	70
K_1	1.00	0.19	79.0	49.0	73
P_1	1.003	0.24	77.0	16.6	64
O_1	1.08	0.264	81.0	43.0	54
M_f	13.66	2.54	250.0	2.9	163
M_{sf}	14.77	13.28	18.8	0.3	164
M_m	27.55	5.04	253.0	1.6	63
S_{sa}	182.62	26.74	256.0	1.5	179
S_a	365.27	19.18	273.0	0.2	179

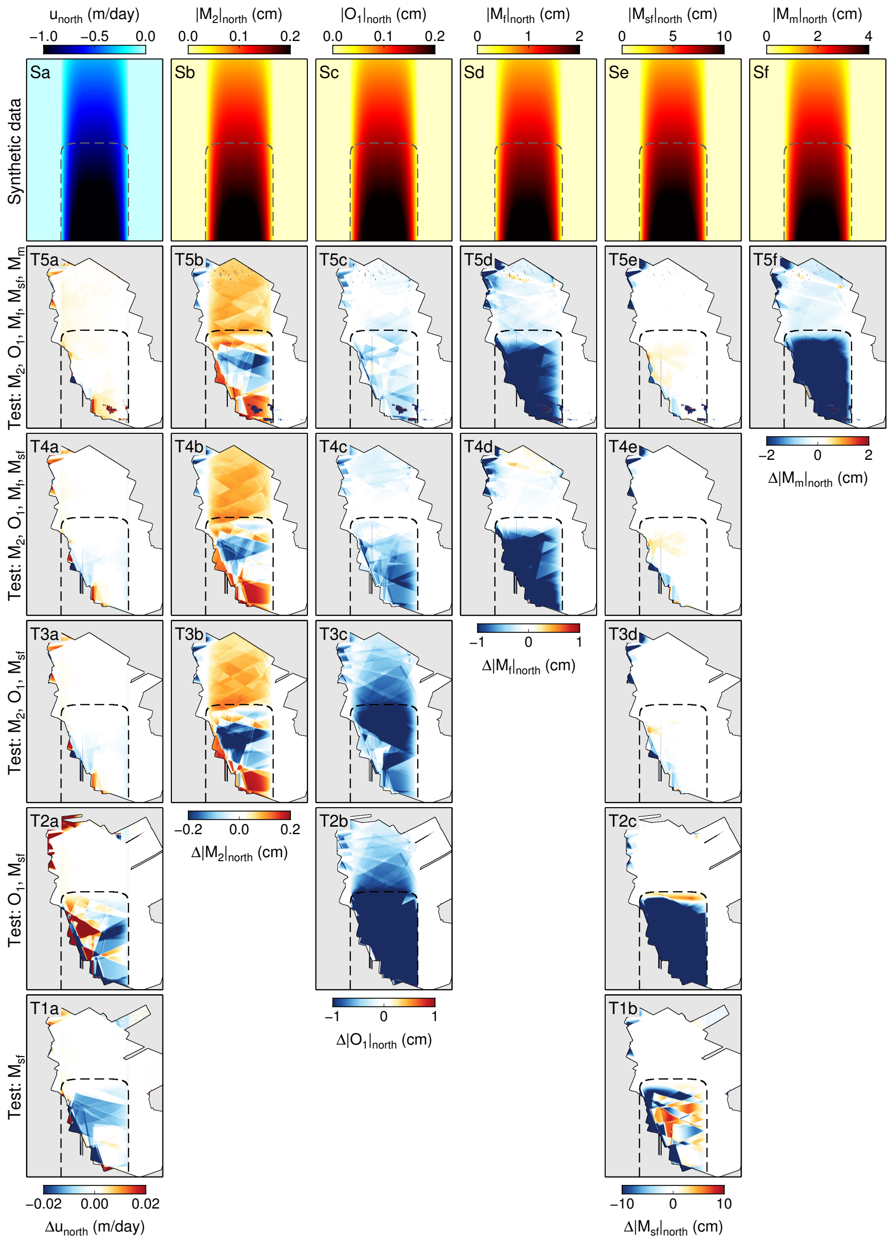

Figure S1. North component of synthetic ice stream flow and tidally induced flow variation amplitudes (Sa–Sf) along with inferred values of ice flow and amplitudes of tidally induced flow variations (T5a–T1b). Rows represent different inversion tests. Tidal constituents considered in each test are given on the left side of the row. Panels within each row are labelled with 'T', the number of tidal constituents in the respective test, and letters in alphabetical order. Columns contain consistent data types. Inferred values for each test are given as the difference between the synthetic ice stream value and the inferred value. All differenced plots in a particular column use the same colormap bounds. Colormaps are scaled to best represent the respective data. Dashed lines in all plots indicate the grounding zone, which bounds the ice shelf.

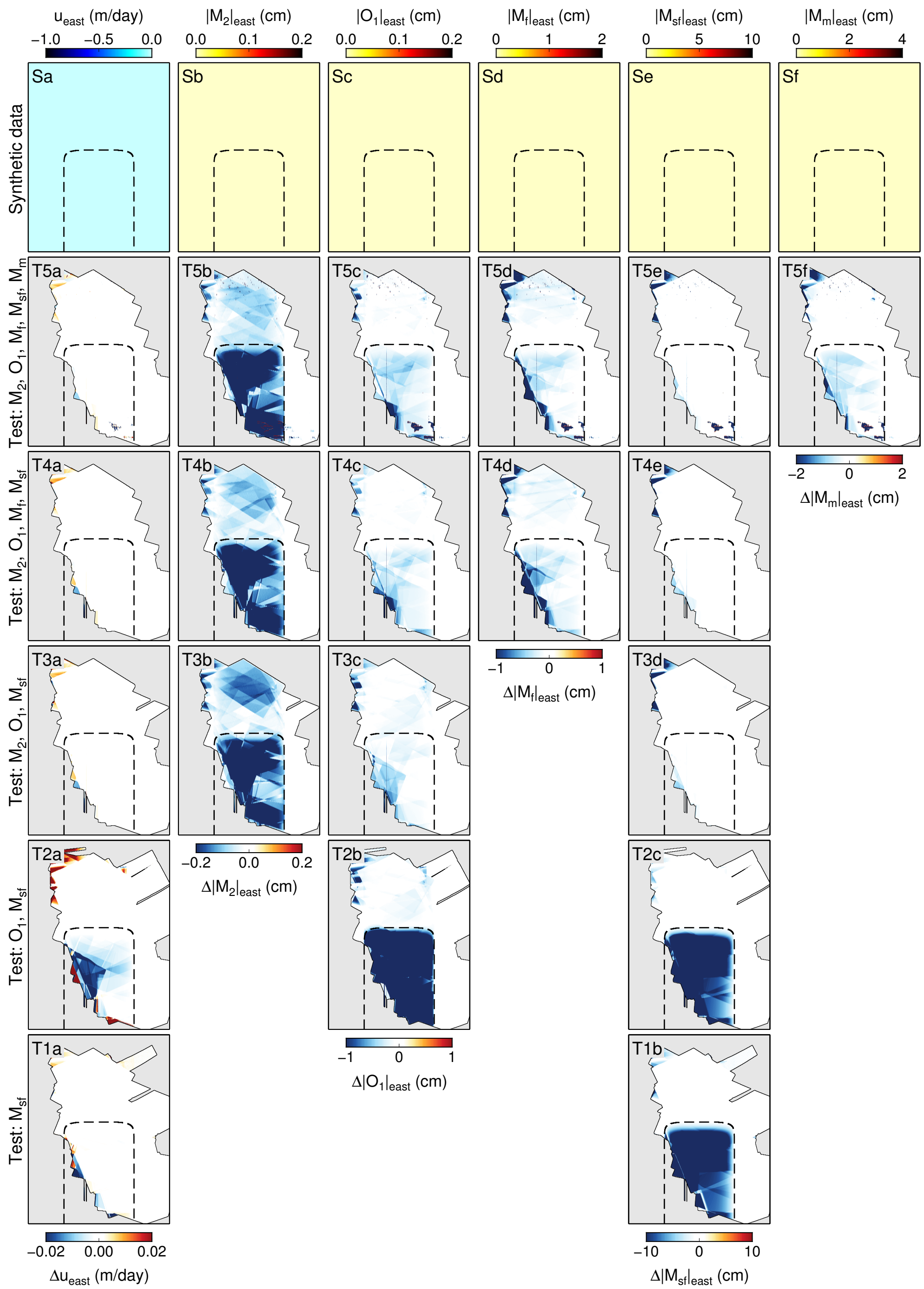

Figure S2. East component of synthetic ice stream flow and tidally induced flow variation amplitudes along with inferred values of ice flow and amplitudes of tidally induced flow variations. Figure layout and labelling follows Fig. S1.

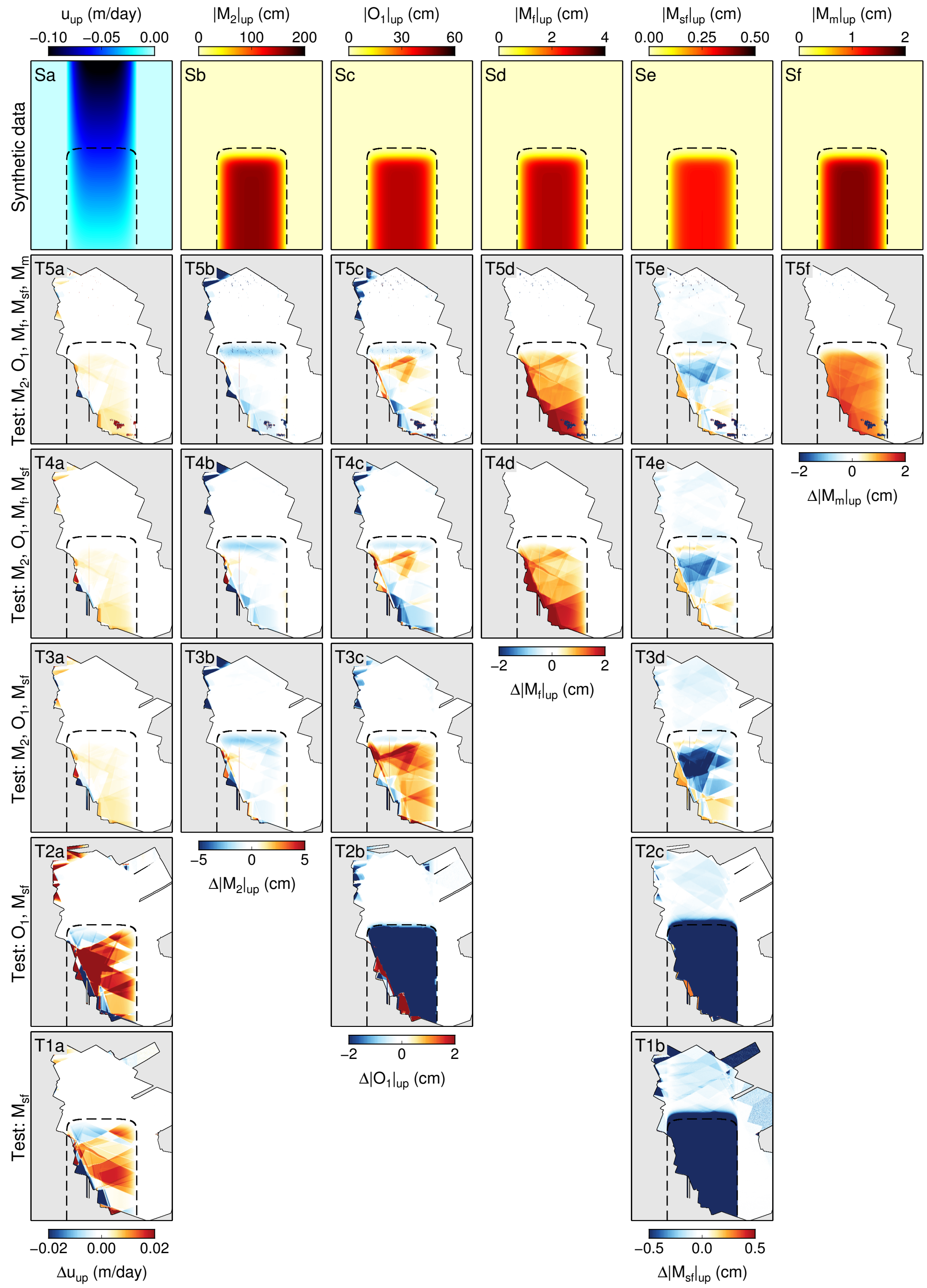

Figure S3. Synthetic data and inferred values of vertical ice motion and tidally induced variations. Figure layout and labelling follows Fig. S1. Positive values in Sa–Sf are upward.

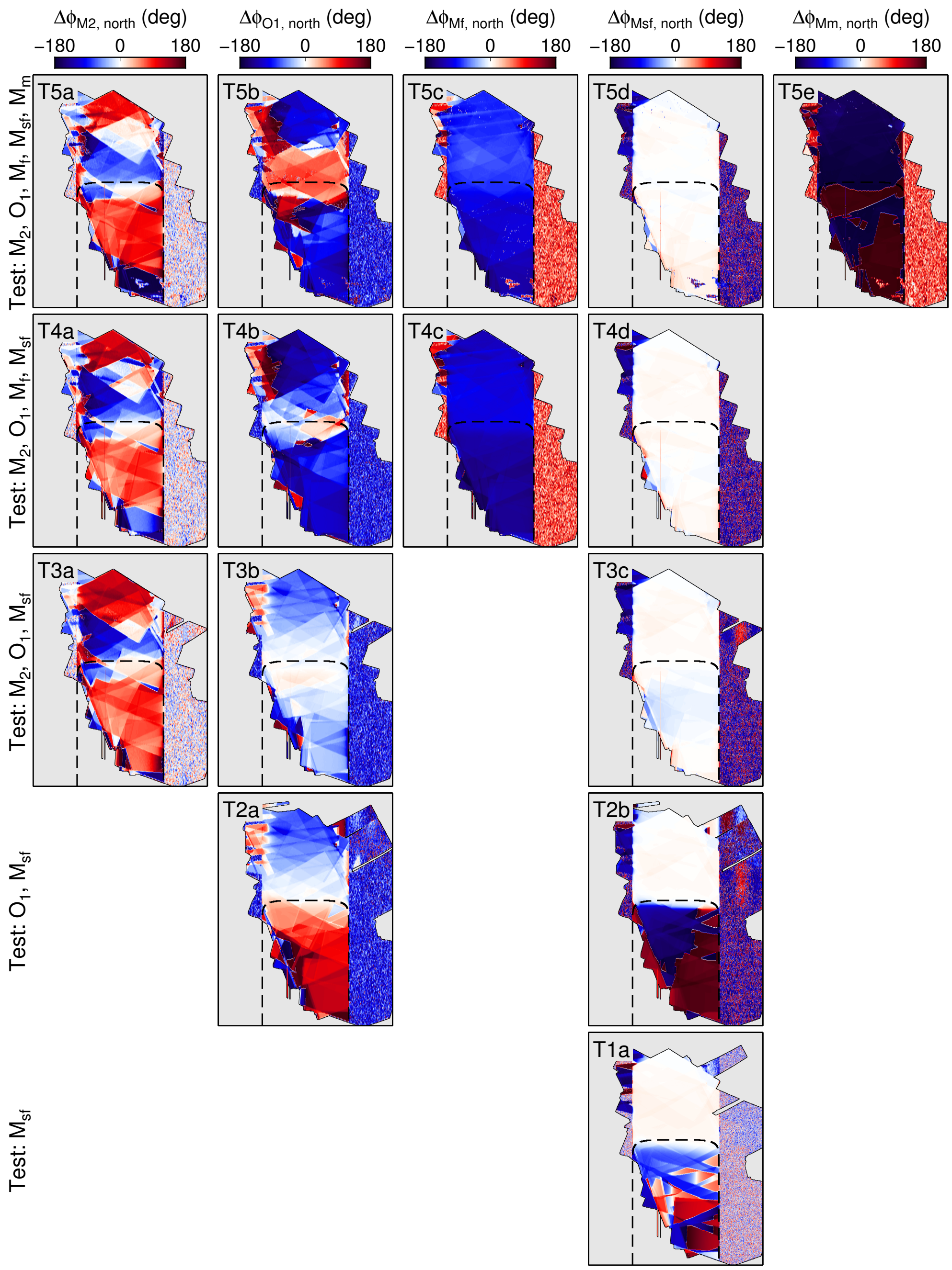

Figure S4. Inferred phase values relative to the respective, spatially constant, synthetic values for the north components. Figure layout and labelling follows Fig. S1.

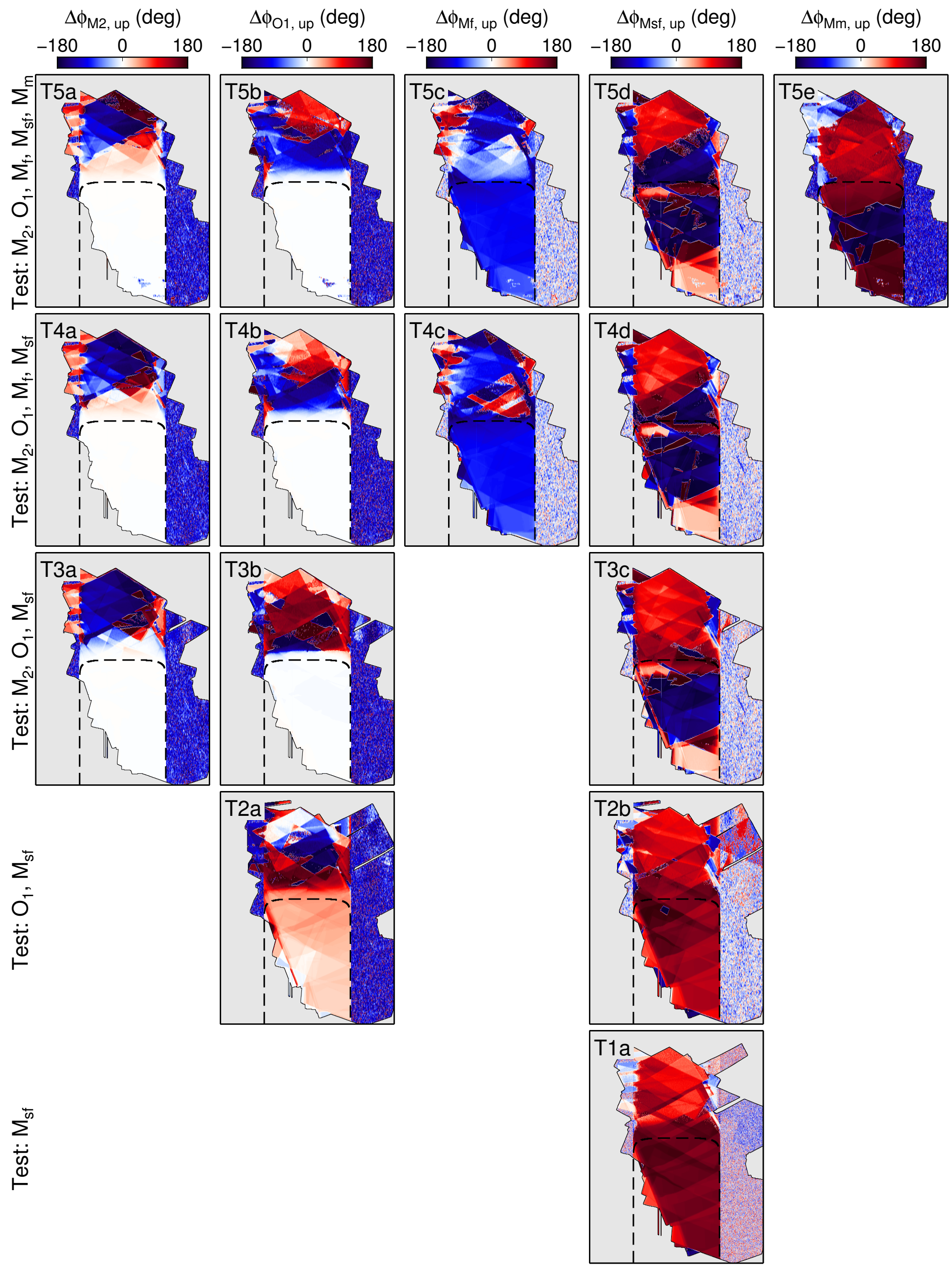

Figure S5. Inferred phase values relative to the respective, spatially constant, synthetic values for the up components. Figure layout and labelling follows Fig. S1.

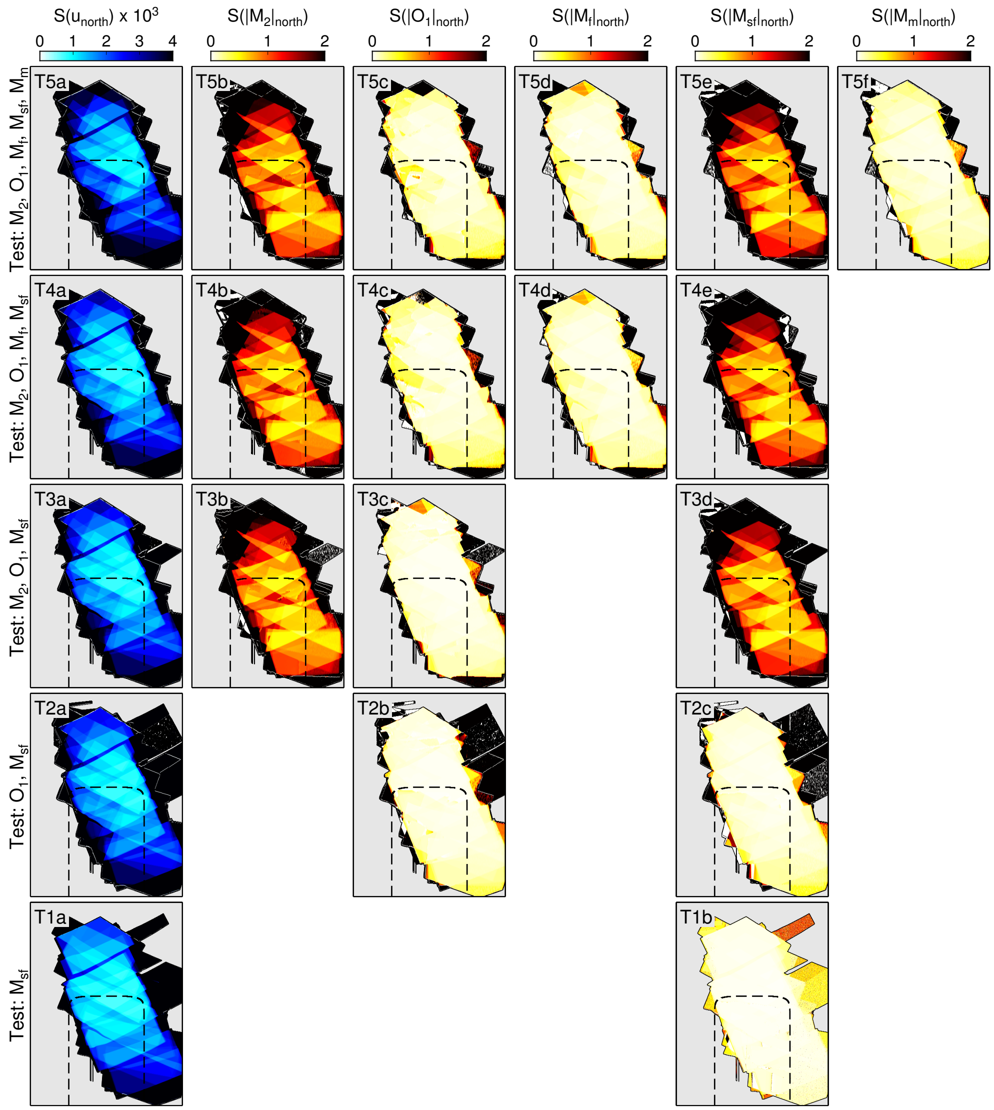

Figure S6. North components of the diagonal elements of the noise-sensitivity matrices, **S**, corresponding to velocity and sinusoidal amplitude for each test case. Figure layout and labelling follows Fig. S1.

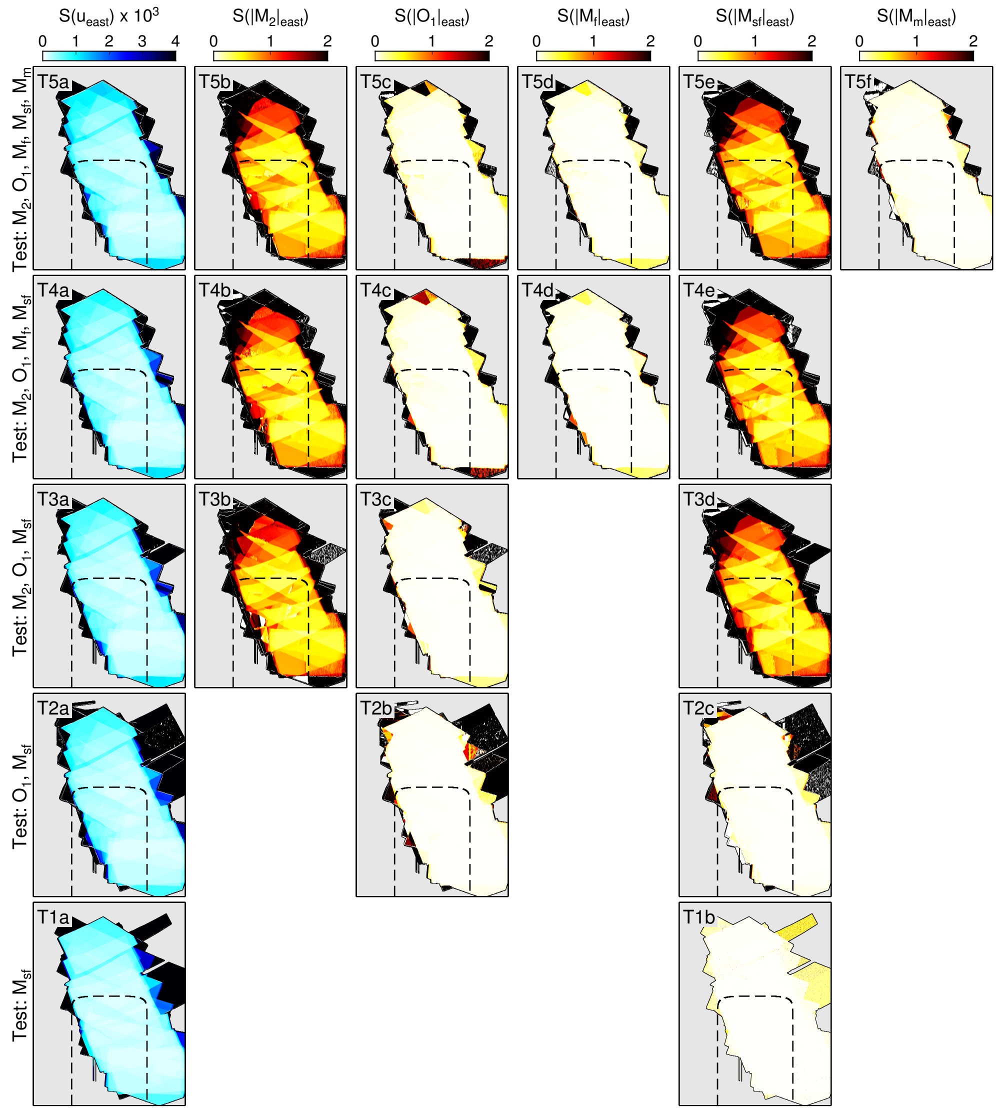

Figure S7. East components of the diagonal elements of the noise-sensitivity matrices, **S**, corresponding to velocity and sinusoidal amplitude for each test case. Figure layout and labelling follows Fig. S1.

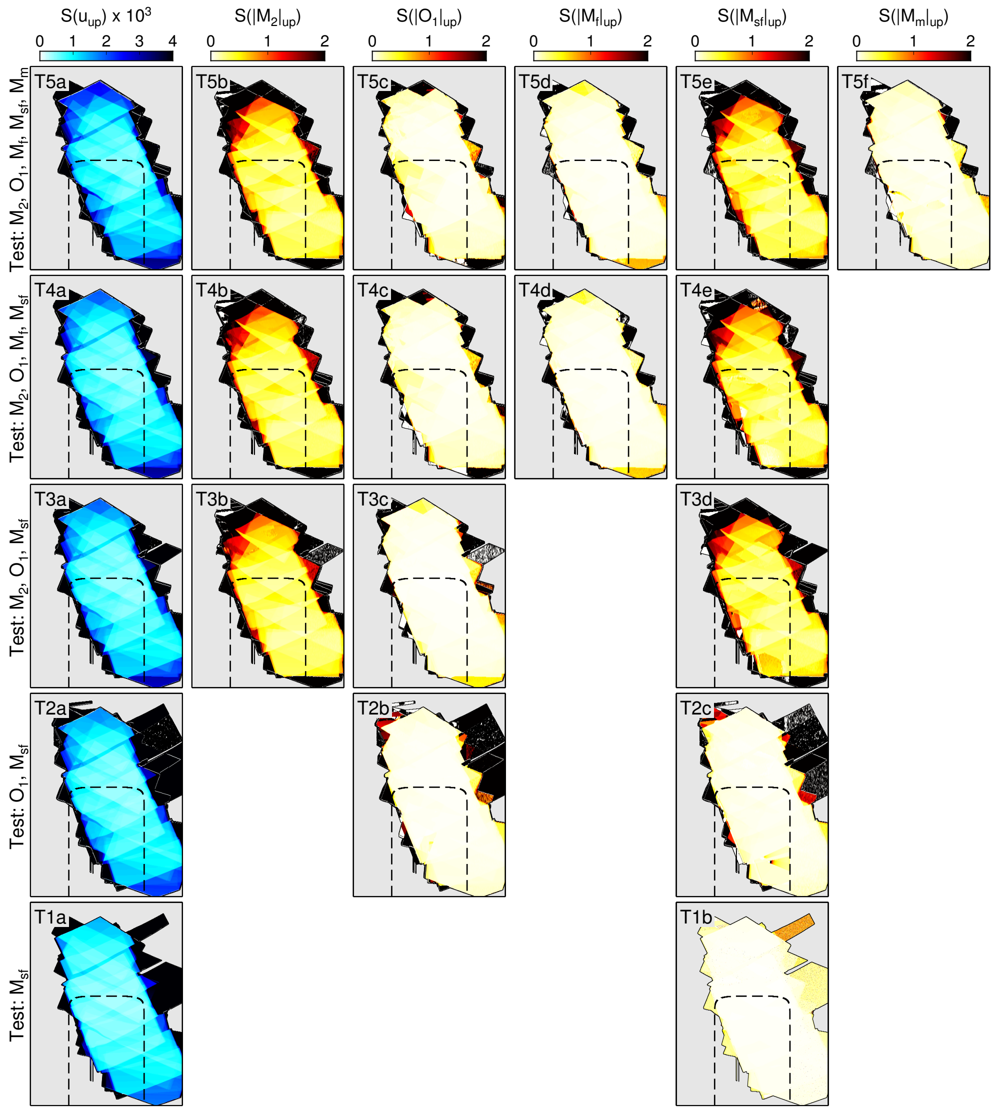

Figure S8. Up components of the diagonal elements of the noise-sensitivity matrices, **S**, corresponding to velocity and sinusoidal amplitude for each test case. Figure layout and labelling follows Fig. S1.

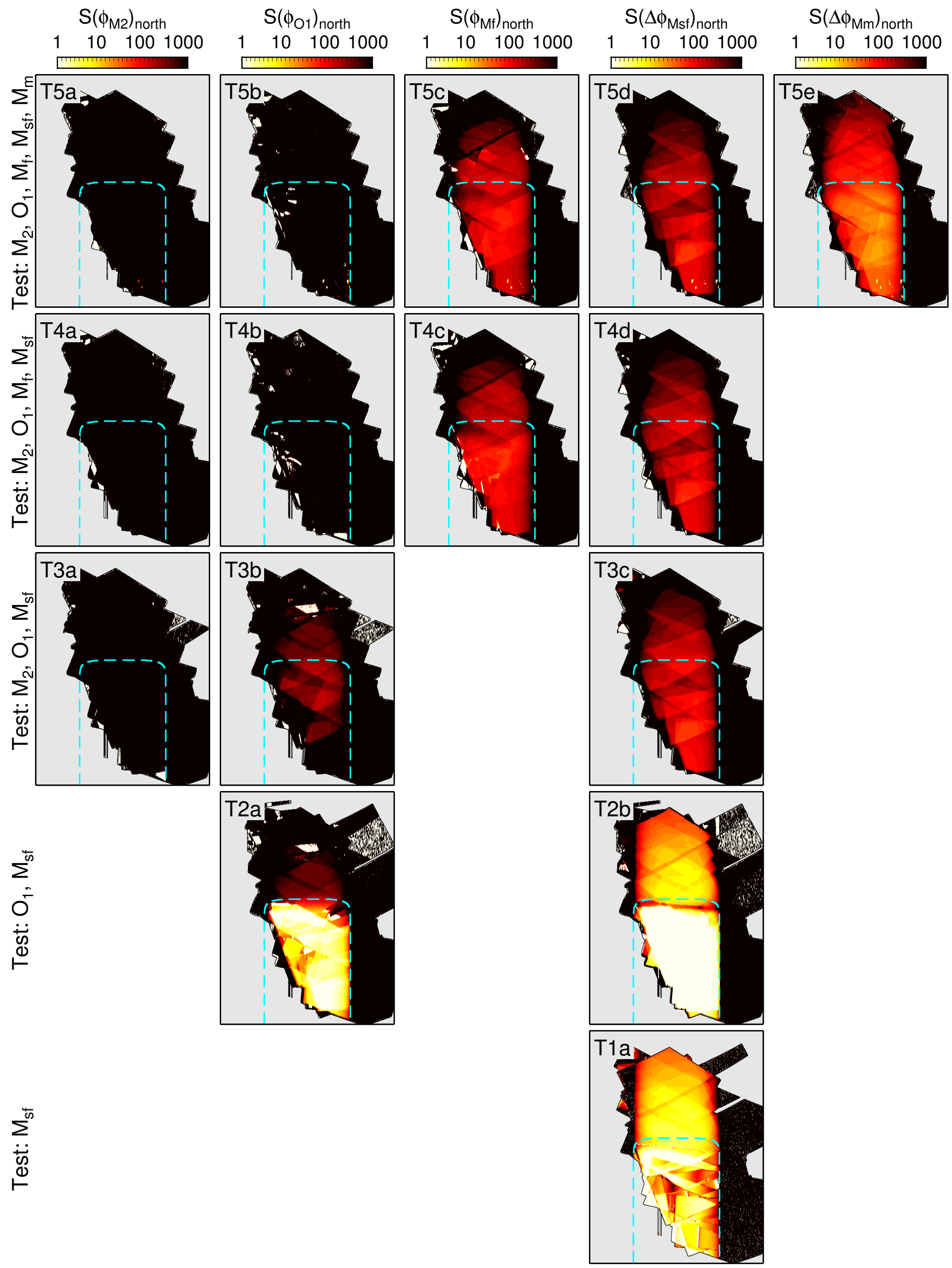

Figure S9. North components of the diagonal elements of the noise-sensitivity matrices, **S**, corresponding to sinusoidal phase for each test case. Figure layout and labelling follows Fig. S1.

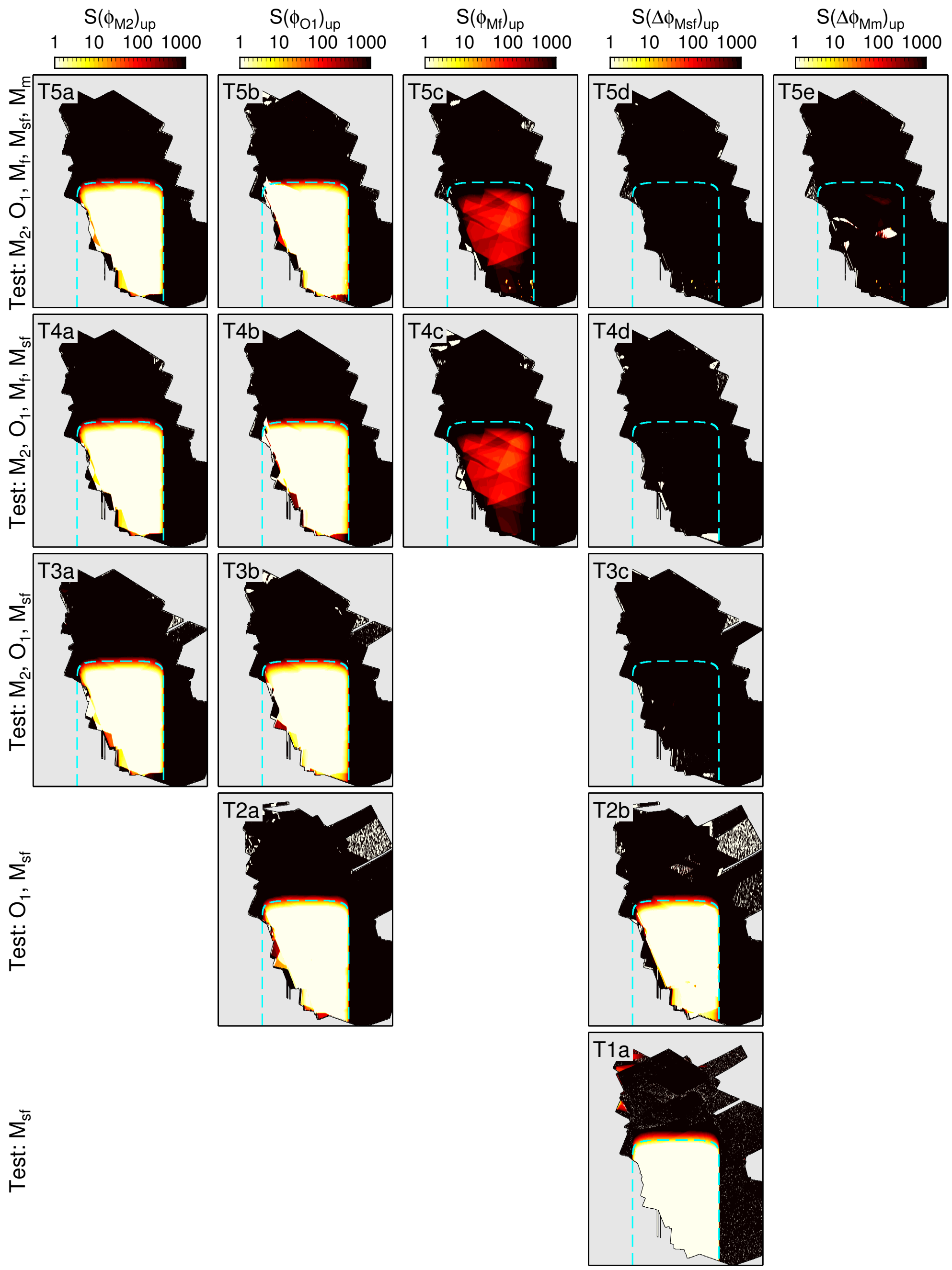

Figure S10. Up components of the diagonal elements of the noise-sensitivity matrices, **S**, corresponding to sinusoidal phase for each test case. Figure layout and labelling follows Fig. S1.

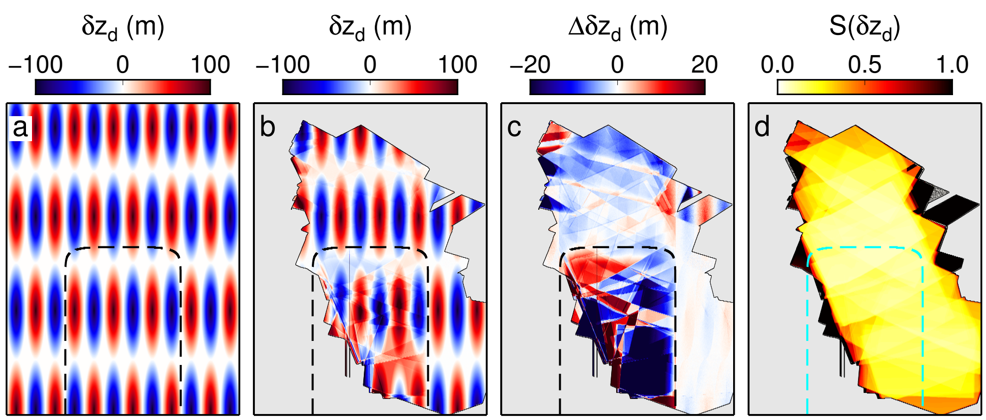

Figure S11. (a) Synthetic topographic residual, (b) inferred topographic residual, (c) misfit topographic residual relative to true value, and (d) topographic component of the diagonal of the noise-sensitivity matrix, **S**. Results shown for the case that includes only M_2, O_1, and M_{sf} tidal constituents.

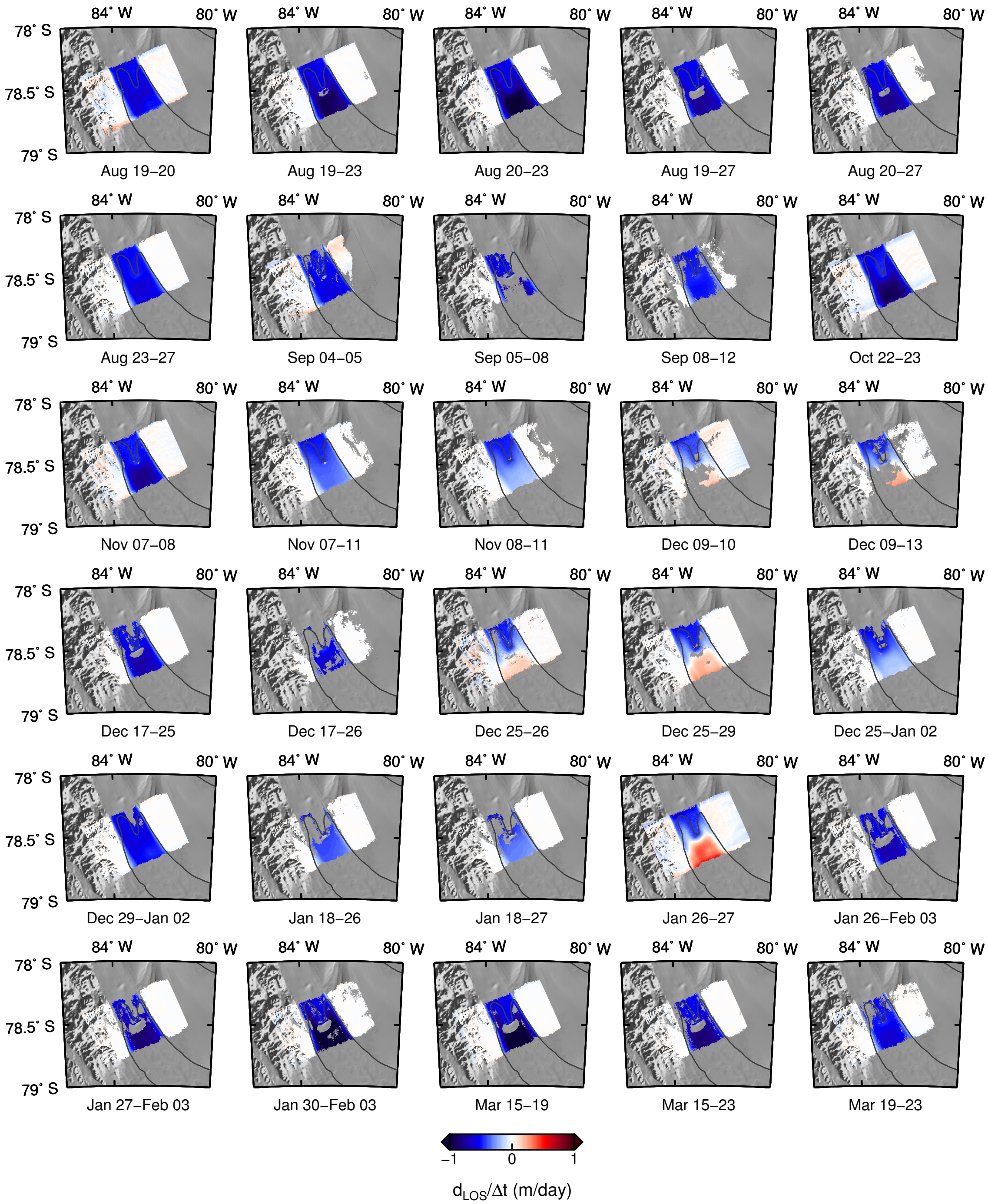

Figure S12. Selected line-of-sight displacement fields (d_{LOS}) along a single CSK track normalized by time between acquisitions (Δt). Negative values indicate motion toward the satellite. Grounding lines are the same as in Fig. 1 and background images are MODIS mosaic of Antarctica (MOA) [*Haran et al.*, 2005; *Scambos et al.*, 2007; *Haran et al.*, 2014].

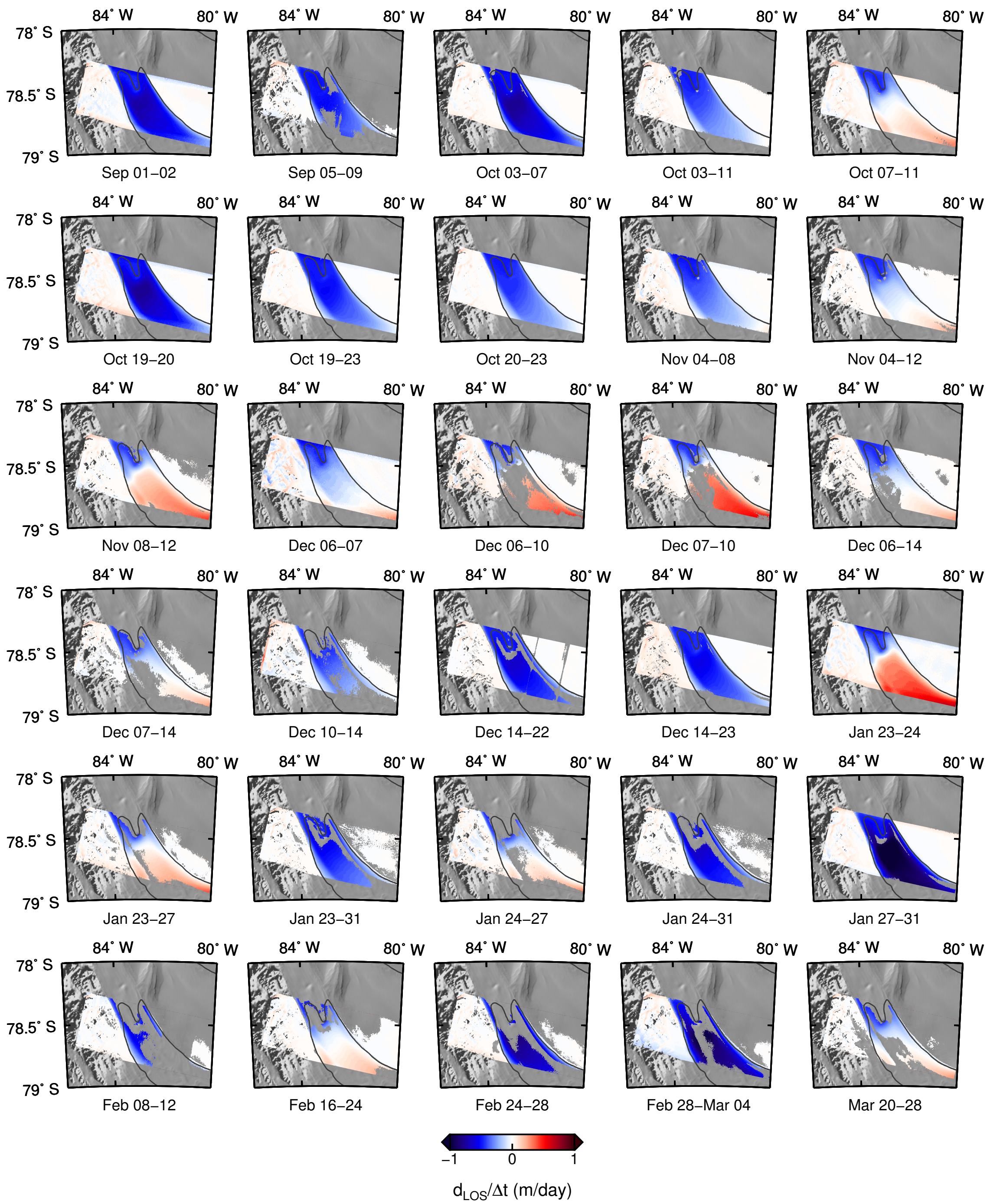

Figure S13. Selected line-of-sight displacement fields (d_{LOS}) along a single CSK track normalized by time between acquisitions (Δt). Negative values indicate motion toward the satellite. Grounding lines are the same as in Fig. 1 and background images are from MOA.

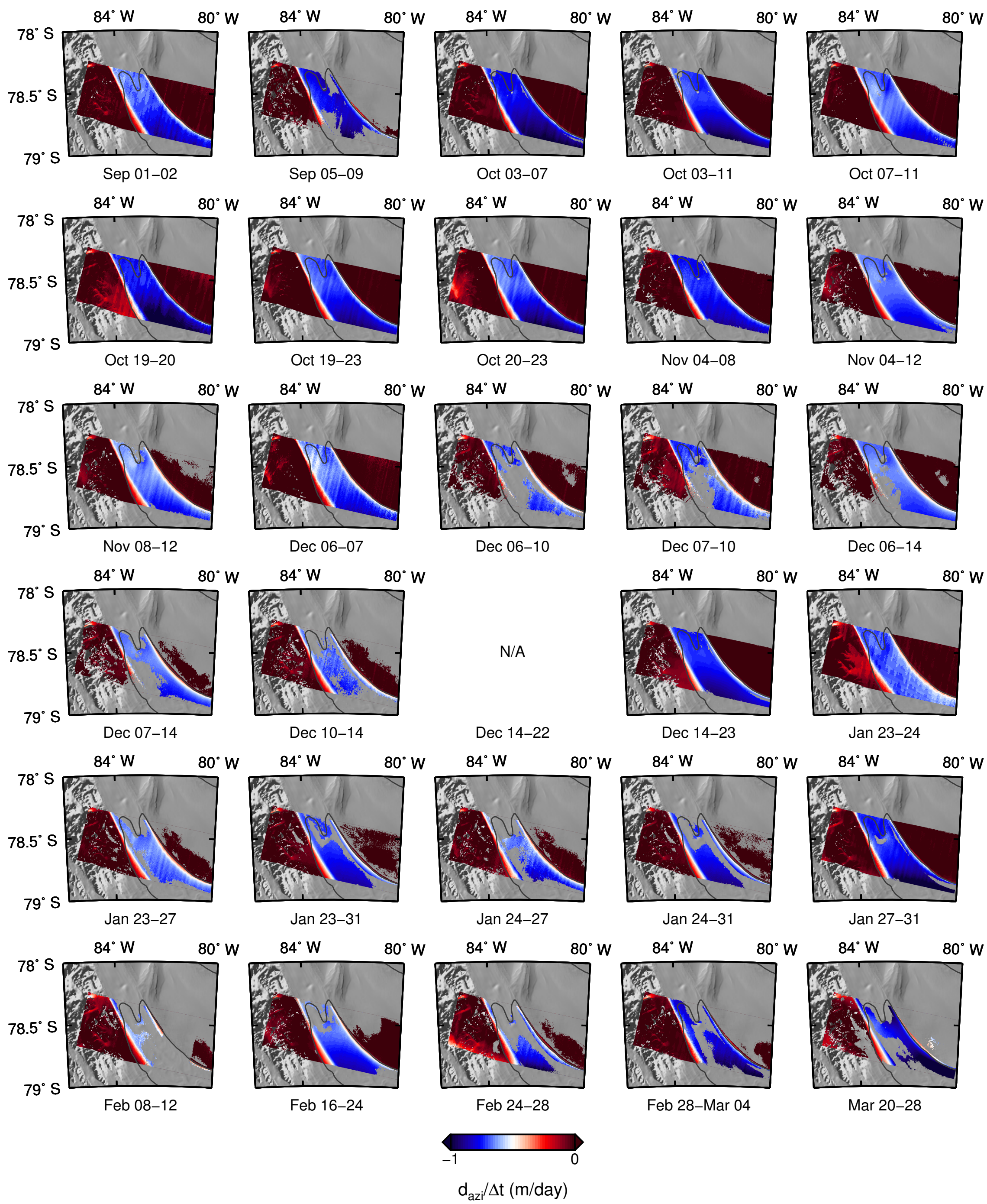

Figure S14. Selected azimuth displacement fields (d_{azi}) along the CSK track shown in Fig. S13 normalized by time between acquisitions (Δt). Negative values indicate motion anti-parallel to the satellite heading vector. Grounding lines are the same as in Fig. 1 and background images are from MOA.

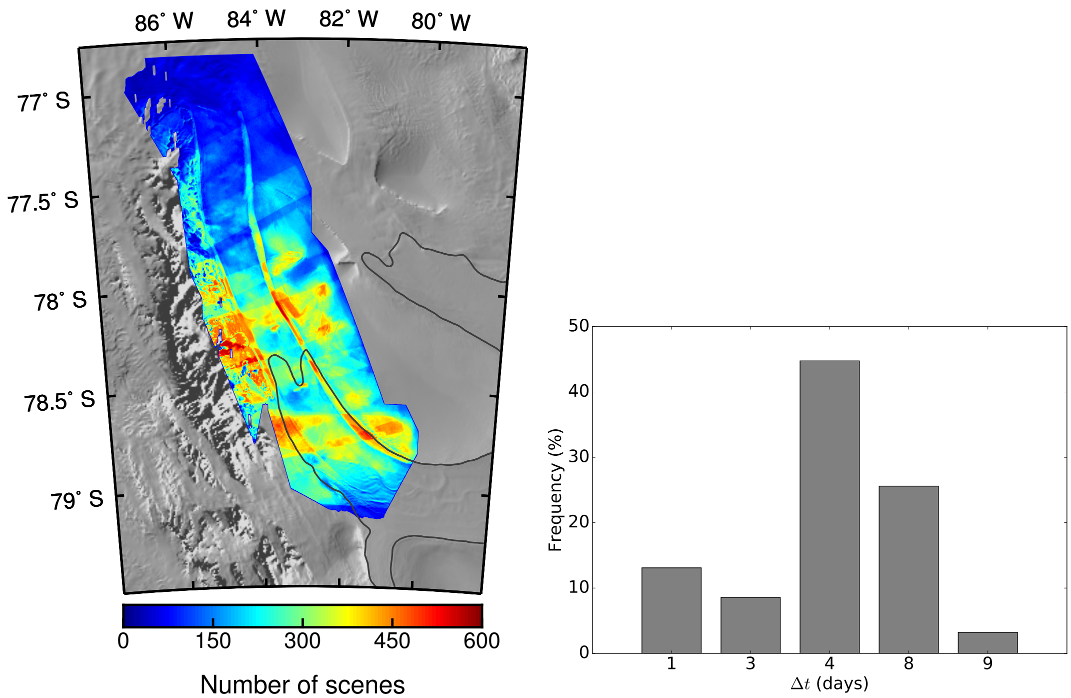

Figure S15. (left) Number of unique, overlapping displacement fields and (right) a histogram of repeat-pass times (Δt_{ab} in Eq. 4) for the displacement fields used to infer time-dependent, 3D velocity fields over RIS.

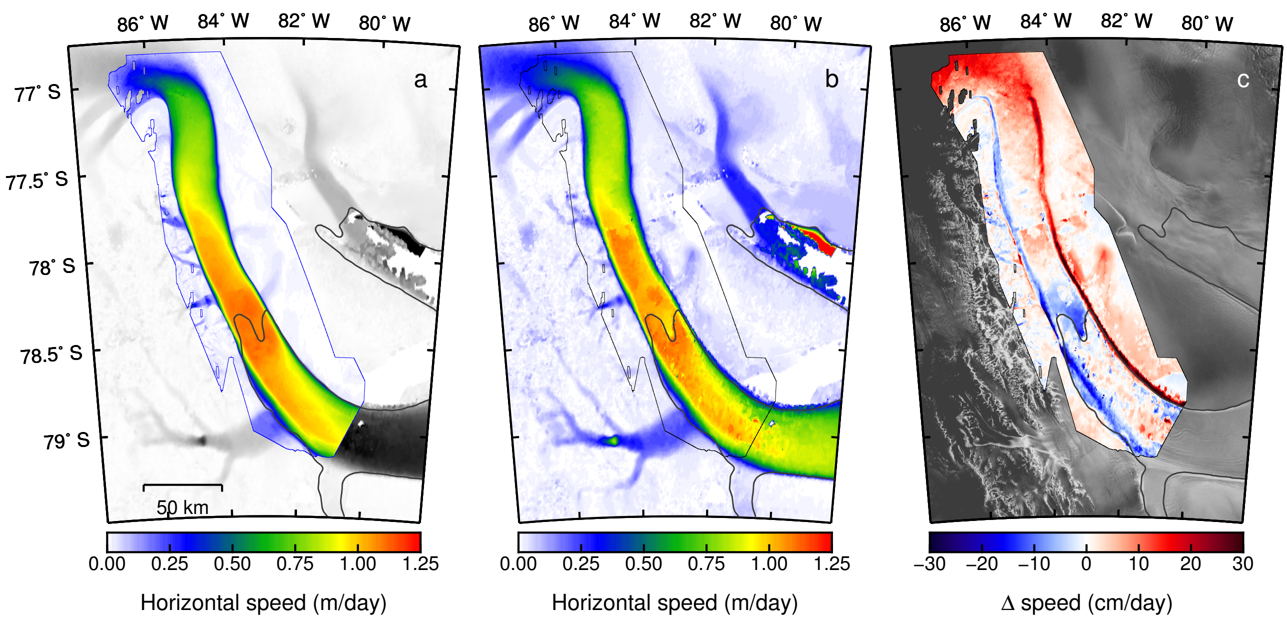

Figure S16. Comparison of SAR-derived secular horizontal velocity fields. (a) Horizontal speed from this study (same as Fig. 5a in the text without vectors). (b) Horizontal speed from *Rignot et al.* [2011]. (c) Horizontal speed in (a) relative to (b) where positive values indicate slower speed in (a). Grayscale background is RADARSAT-1 AMM-1 [*Jezek et al.*, 2013]. Grounding lines are the same as in Fig. 1.

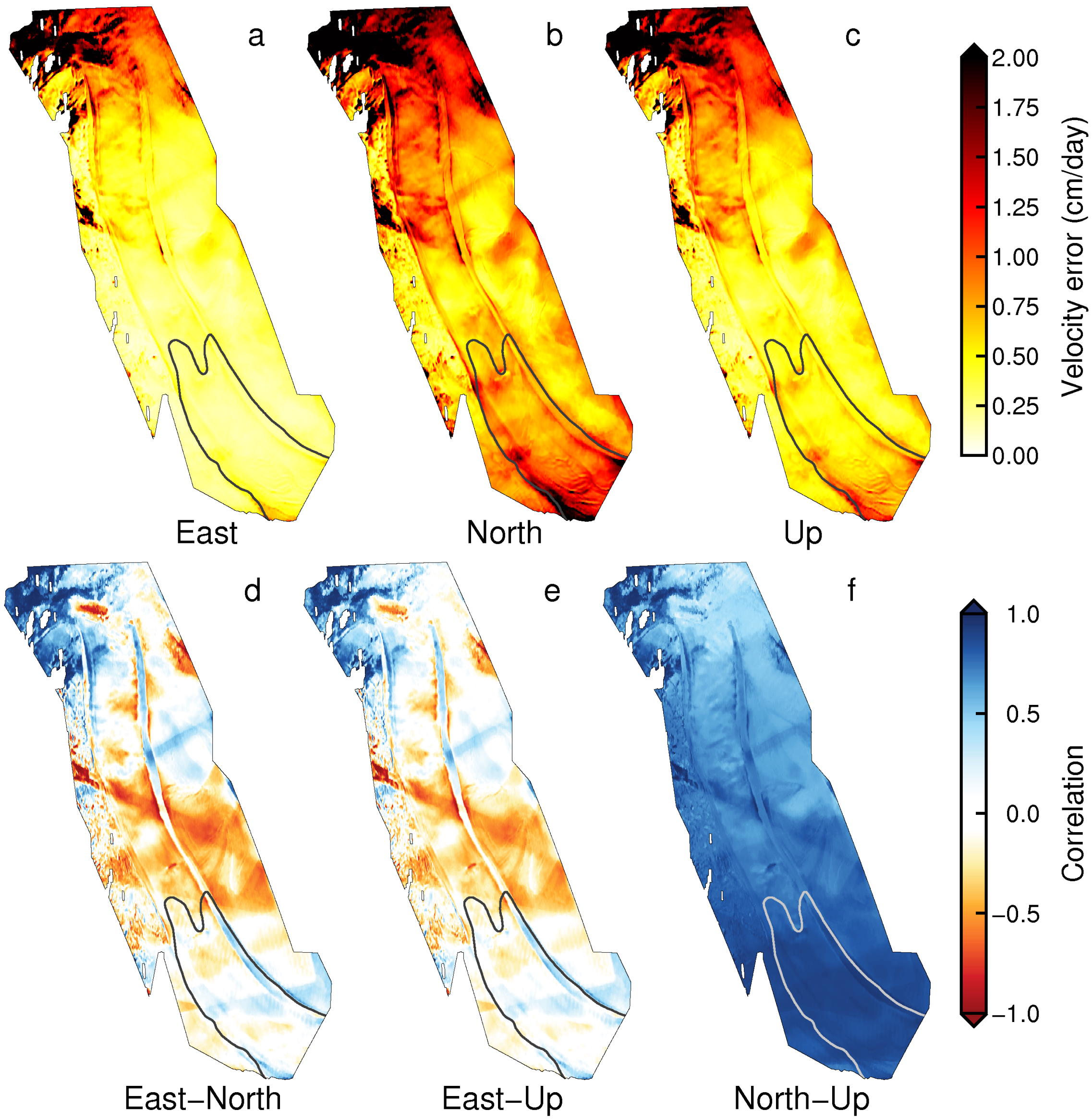

Figure S17. Formal errors and correlation in secular velocity components calculated from the posterior model covariance matrix, $\widetilde{\mathbf{C}}_m$. (a–c) Formal errors for (a) east, (b) north, and (c) up velocity components. Note that the error scale is cm/day, meaning that errors within the ice stream rarely exceed 5% of the observed velocity. (d–f) Correlation between (d) east and north, (e) east and up, and (f) north and up secular velocity components. Grounding lines are the same as in Fig. 1.

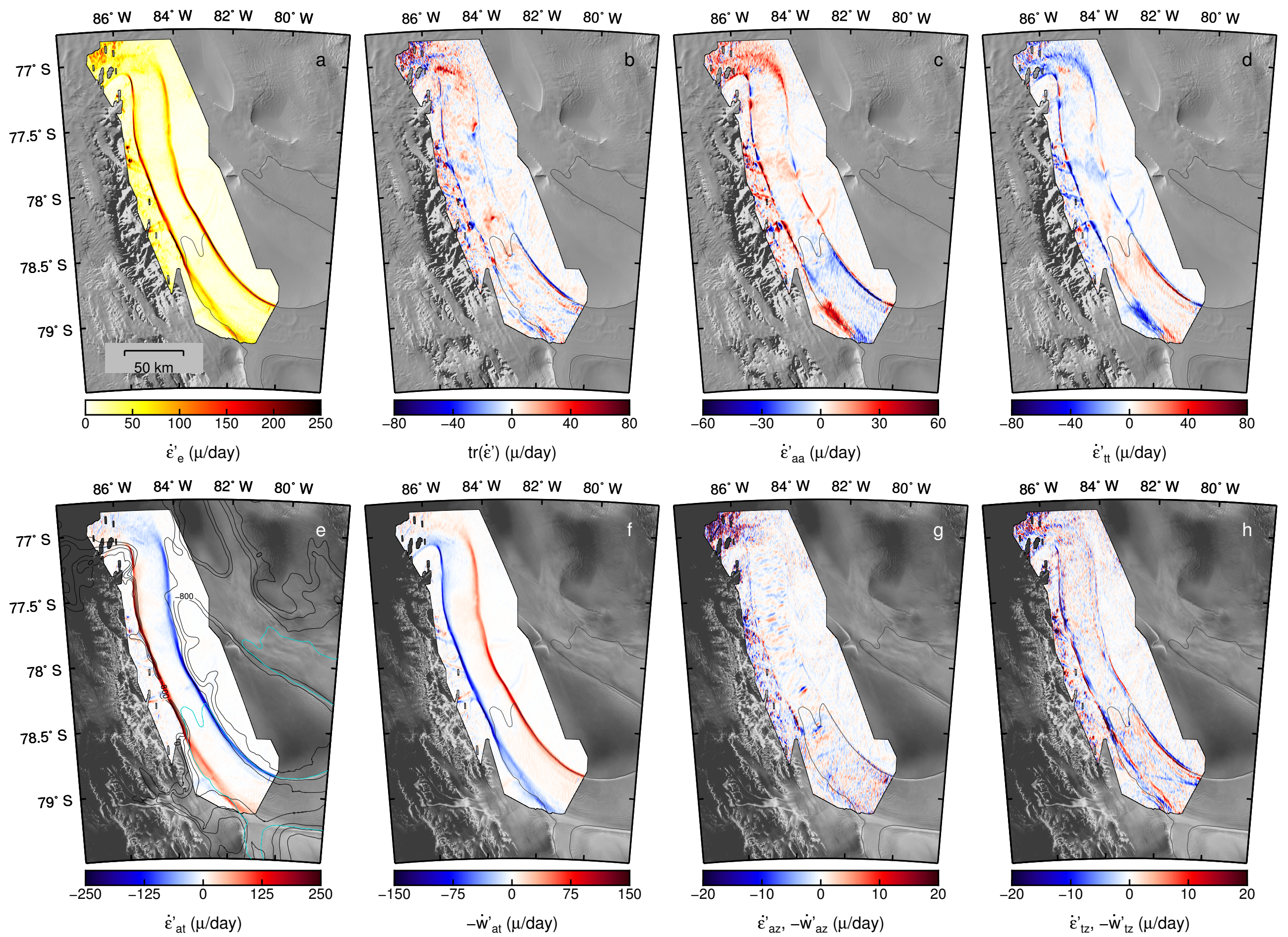

Figure S18. Unique, nonzero components of the micro ($\mu = 10^{-6}$) secular strain rate and rotational tensors. All values are given in a local along-flow (subscript a), transverse- or across-flow (subscript t), up (subscript z) coordinate system. (a–b) Strain rate tensor invariants: (a) effective strain rate and (b) velocity divergence, assuming $\dot{\varepsilon}_{zz} \ll \dot{\varepsilon}_{aa} + \dot{\varepsilon}_{tt}$. (c) Along-flow and (d) across-flow deviatoric normal strain rates. (e) Lateral shear strain rate and (f) lateral rotation rate. Contour lines in (e) are bathymetry from Bedmap2. (g–h) Vertical shearing and rotation (g) along flow and (h) across flow. Background grayscale images are (a–d) MODIS mosaic of Antarctica [*Haran et al.*, 2005; *Scambos et al.*, 2007; *Haran et al.*, 2014] and (e–h) RADARSAT-1 AMM-1 mosaic. Grounding lines are the same as in Fig. 1.

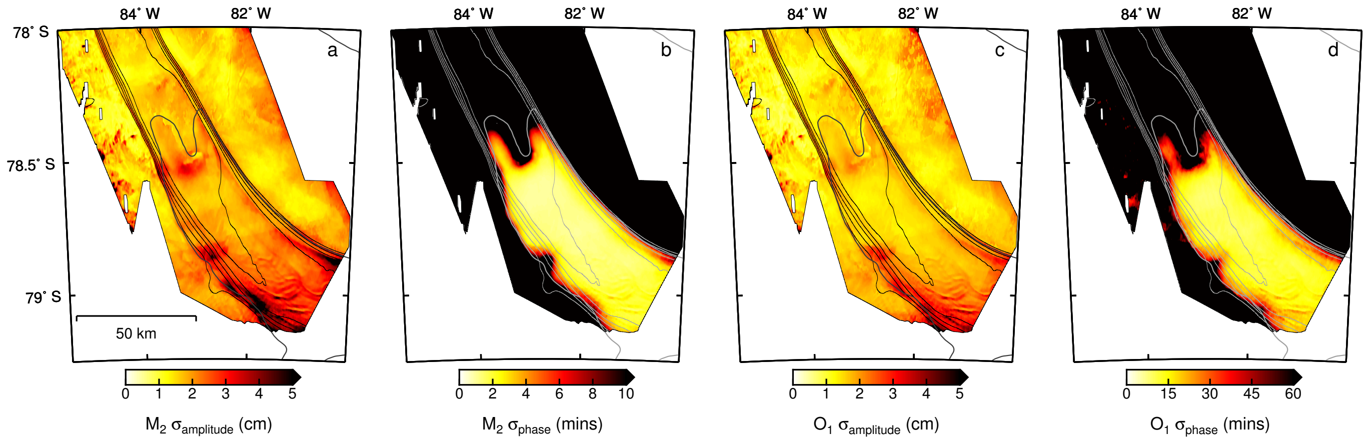

Figure S19. Formal errors in time-dependent vertical velocity components. (a–b) Standard deviation of vertical M_2 amplitude and phase, respectively. (c–d) Standard deviation of vertical O_1 amplitude and phase, respectively. Grounding lines are the same as in Fig. 1 and thin contour lines show horizontal secular speed in 0.2 m/day increments.

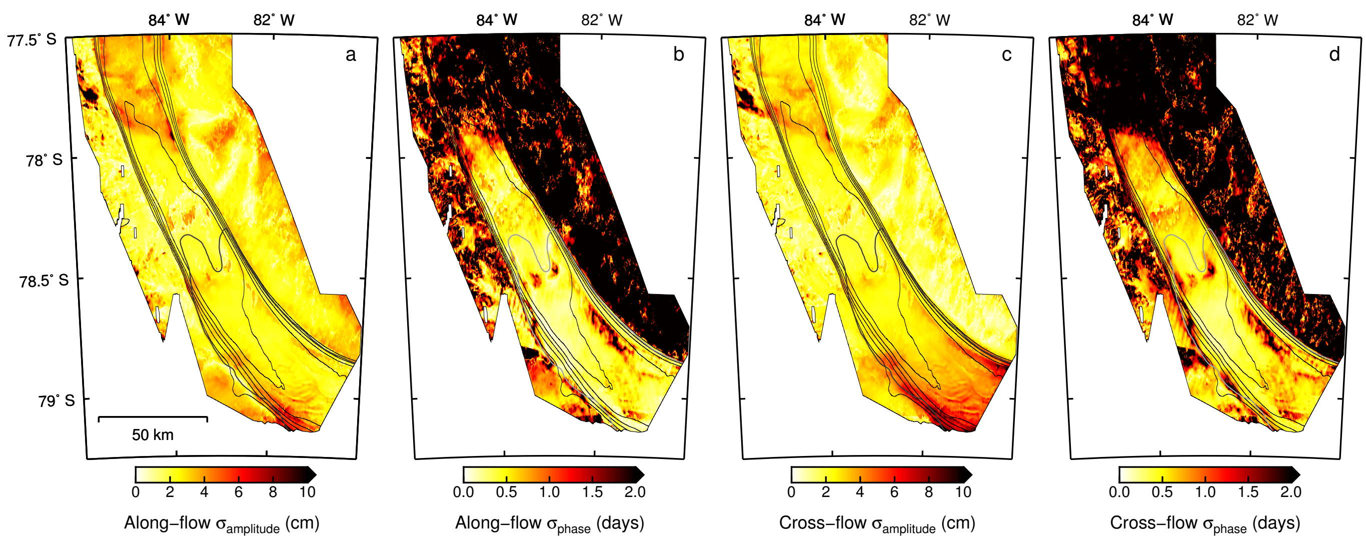

Figure S20. Formal errors in time-dependent horizontal velocity components. (a–b) Standard deviation of along-flow M_{sf} amplitude and phase, respectively. (c–d) Standard deviation of cross-flow M_{sf} amplitude and phase, respectively. Grounding lines are the same as in Fig. 1 and thin contour lines show horizontal secular speed in 0.2 m/day increments.